An Estimate of the Lorenz Energy Cycle for the World Ocean Based on the 1/10° STORM/NCEP Simulation

JIN-SONG VON STORCH,* CARSTEN EDEN,+ IRINA FAST,# HELMUTH HAAK,* DANIEL HERNÁNDEZ-DECKERS,*,@ ERNST MAIER-REIMER,* JOCHEM MAROTZKE,* AND DETLEF STAMMER+

* *Max-Planck Institute for Meteorology, Hamburg, Germany*
+ *Institute of Oceanography, University of Hamburg, Hamburg, Germany*
# *German Climate Computing Center, Hamburg, Germany*
@ *Climate Change Research Centre, University of New South Wales, Sydney, New South Wales, Australia*

(Manuscript received 3 May 2012, in final form 8 August 2012)

ABSTRACT

This paper presents an estimate of the oceanic Lorenz energy cycle derived from a 1/10° simulation forced by 6-hourly fluxes obtained from NCEP–NCAR reanalysis-1. The total rate of energy generation amounts to 6.6 TW, of which 1.9 TW is generated by the time-mean winds and 2.2 TW by the time-varying winds. The dissipation of kinetic energy amounts to 4.4 TW, of which 3 TW originate from the dissipation of eddy kinetic energy. The energy exchange between reservoirs is dominated by the baroclinic pathway and the pathway that distributes the energy generated by the time-mean winds. The former converts 0.7 to 0.8 TW mean available potential energy to eddy available potential energy and finally to eddy kinetic energy, whereas the latter converts 0.5 TW mean kinetic energy to mean available potential energy.

This energy cycle differs from the atmospheric one in two aspects. First, the generation of the mean kinetic and mean available potential energy is each, to a first approximation, balanced by the dissipation. The interaction of the oceanic general circulation with mesoscale eddies is hence less crucial than the corresponding interaction in the atmosphere. Second, the baroclinic pathway in the ocean is facilitated not only by the surface buoyancy flux but also by the winds through a conversion of 0.5 TW mean kinetic energy to mean available potential energy. In the atmosphere, the respective conversion is almost absent and the baroclinic energy pathway is driven solely by the differential heating.

1. Introduction

A quantitative description of the oceanic energy cycle is crucial for improving our understanding about how the ocean general circulation functions. For the atmosphere, the Lorenz energy cycle (LEC) has been proven to be a useful concept for analyzing dynamical processes (Lorenz 1955; Oort and Peixoto 1983). It is well accepted that the atmosphere works as a heat engine that operates between warm sources at low latitudes near the surface and cold sinks at high latitudes in the upper atmosphere, thereby performing work to maintain the kinetic energy of the circulations against a continuous drain of energy by frictional dissipation (Oort and Peixoto 1983). The idea of the climate as a heat engine has been more thoroughly discussed by other authors (Johnson 2000; Tailleux 2009, 2010; Lucarini 2009). Given the fact that the ocean is driven by air–sea fluxes from the top, it is generally expected that its energy cycle differs from that in the atmosphere. Peixoto and Oort (1992) pointed out that ''the ocean currents are driven mainly by atmospheric forcing of the winds rather than by internal conversions in the oceans themselves'' as in case of the atmosphere. Following Sandstrom's theorem (Sandström 1908, 1916), Huang (2004) claimed that ''the ocean is not a heat engine.'' Apart from these general considerations, a detailed description of oceanic energetics that illustrates how the oceanic LEC differs from the atmospheric one has been lacking.

One difficulty is due to the limited temporal and spatial coverage of oceanic observations. Peixoto and Oort (1992) estimated various energy components and some

Corresponding author address: Jin-Song von Storch, Max-Planck Institute for Meteorology, Bundesstraße 53, 20146 Hamburg, Germany.
E-mail: jin-song.von.storch@zmaw.de

DOI: 10.1175/JPO-D-12-079.1

energy generation and conversion terms, partially by vertically extrapolating available surface data down to the oceanic interior. The picture obtained cannot depict the detailed pathways of the oceanic LEC. It is not clear, apart from the dominant role of the winds in generating kinetic energy, what it is that characterizes the ocean as not being a heat engine. More recently, an updated schematic of oceanic energy reservoirs, sources, sinks, and transfer routes has been put forward by Ferrari and Wunsch (2009, 2010). To avoid complications related to the question of how much potential and internal energies are available and can be converted into kinetic energy, Ferrari and Wunsch concentrated on the ocean circulation kinetic energy, which can be decomposed into the kinetic energies of the time-mean circulation, geostrophic eddies and internal waves, and the rate of their generation and transfer toward dissipation. Even by leaving out the issue of available potential energy, whose definition is arguable, many of the numbers in the picture provided by Ferrari and Wunsch are highly uncertain.

Another approach that helps to improve our understanding of oceanic energetics is to perform numerical simulations using eddy-resolving OGCMs, despite the biases related to these estimates (Lucarini and Ragone 2011), and to infer the energy cycle from the output of these simulations. This activity has long been developed, starting from the pioneering work by Cox (1985) to studies using ''mesoscale eddy-permitting'' models, mostly for parts of the World Ocean (for a review of high-resolution simulations see, e.g., Böning and Semtner 2001, for LEC derived from simulations of various parts of the World Ocean see Olbers et al. 2012). It is only recently that global simulations with a horizontal resolution of one tenth of degree or finer have become possible. Several global (near-global) simulations over time periods of more than one decade have been performed (e.g., Masumoto et al. 2004; Sasaki et al. 2004, 2008; Maltrud and McClean 2005; Lee et al. 2007; Maltrud et al. 2010). The underlying OGCMs are formulated using a realistic geometry and bathymetry of the World Ocean and have been run in uncoupled mode, forced by realistic conditions at the sea surface. While these simulations have proven to realistically produce many features of the oceanic general circulation, what remains missing is a study of the full energy cycle of the global ocean.

To make further progress in analyzing the LEC in the ocean, we ran the Max-Planck Institute Ocean Model (MPI-OM) with a $^1/_{10}$ degree horizontal resolution, driven by realistic forcing provided by the National Centers for Environmental Prediction (NCEP)–National Center for Atmospheric Research (NCAR) reanalysis-1. Different from most of the previous efforts, we archived the all relevant second-moment statistics by accumulating two-variable-products at every model time step. Equipped with this second-moment information, we provide below a first complete estimate of the LEC for the global ocean that describes the time-mean balances among four energy reservoirs: K_m and P_m, the kinetic and available potential energy of the time-mean circulation, and K_e and P_e, the mean kinetic and available potential energy of the time-varying circulation.

The structure of the remaining paper is as follows. A brief description of the STORM/NCEP simulation is given in section 2. Section 3 summarizes the definitions of the four reservoirs and the terms describing the generations of and exchanges among the reservoirs. Section 3 also discusses the extent to which the terms in the oceanic LEC are affected by the choice of the reference density needed to define the available potential energy. According to the formulation given in section 3, results regarding the energy reservoirs, the generation, and dissipation of and the exchanges among the reservoirs are presented in sections 4–7. Section 8 provides an overall picture of LEC of the simulated ocean. Through a comparison with the atmospheric LEC, the questions of how the oceanic LEC differs from that of the atmosphere and what makes the ocean being not a heat engine are addressed. A summary and concluding remarks are given in section 9.

2. The STORM/NCEP simulation

Within the German consortium project STORM, which aims at a high-resolution coupled climate change simulation, we replaced the bipolar grid of the MPI-OM model by a tripolar grid to ensure an essentially isotropic horizontal resolution. The tripolar MPI-OM used for the present study has a horizontal resolution of about 0.1 degree at the equator. North of the equator, the grid is a lattice of families of ellipses and their orthogonal trajectories with ''North Pole'' being represented by a line having two foci lying on the same latitude shifted by 180 degrees in longitude in North America and Asia. South of the equator, the grid is Mercator and has a grid size of $^1/_{10}° \times \cos(\phi)$, where ϕ is latitude. Thus, the model resolution is smaller than 5 km south of 60°S, with the smallest grid size being 2.3 km. The total number of horizontal grid points is 3600×2392. In the vertical, the model has 80 levels. The thickness of these layers, which is about 10–15 m in the first 200 m, increases gradually to 195 m at about 4160-m depth and reaches 279 m for the deepest level at 6038 m. Hereafter, the model is referred to as the MPI-OM/TP6ML80

(TP = tripolar, 6M = 6 min, and L80 = 80 vertical levels). MPI-OM/TP6ML80 is based on the same discretized primitive equations for a hydrostatic Boussinesq fluid and has essentially the same physics as its bipolar predecessor (Jungclaus et al. 2006). The model is coupled to a sea ice model that includes the dynamics of sea ice circulation, the thermodynamics of sea ice growth and melt, and the thermohaline coupling to the ocean model (brine rejection). For the present study, the GM-parameterization for mesoscale eddies is switched off, and the tidal forcing is not activated. Further information on the STORM simulation can be found in von Storch et al. (2012, manuscript submitted to *J. Adv. Model. Earth Syst.*).

The model was spun up for 25 years using the German Ocean Model Intercomparison Project (OMIP) forcing derived from the 15-yr European Centre for Medium-Range Weather Forecasts (ECMWF) Re-Analysis (ERA-15), consisting of a climatological mean forcing plus a daily forcing that describes synoptic variations in year 1982 and is repeatedly applied (Röske 2006). After the 25-year spinup phase, the kinetic energy in the deep ocean reaches a quasi-steady state (not shown). The forcing was then switched to the 6 hourly NCEP–NCAR reanalysis-1 (Kalnay et al. 1996) for the period 1948–2010. The resulting run will be referred to as the STORM/NCEP simulation. It is noted that the NCEP–NCAR reanalysis has notable deficiencies near the surface. The quality is particularly poor over the Southern Ocean, which may impact the surface forcing over the Antarctic Circumpolar Current (ACC).

The STORM/NCEP simulation is one of a few global real-time simulations at a horizontal resolution of about one tenth of degree that is preceded by a multidecadal spinup run and covers much longer than one decade. Such long simulations are required to achieve a quasi-steady state of mesoscale eddies, a necessary condition for estimating the LEC in its steady state.

In addition to standard model output, two-variable products xy are accumulated at every model time step (i.e., every 600 s) to obtain $\overline{xy}$. Here and in the following, the overbar denotes time-averaged values. In case in which x represents one of the three components of the velocity $\mathbf{u} = (u, v, w)$ and y a tracer (temperature or salinity), $\overline{xy}$ represents the mean flux of y in the direction of x. By archiving $\overline{xy}$ as well as $\overline{x}$ and $\overline{y}$, we are able to derive the mean eddy flux $\overline{x'y'}$ from the equality

$$\overline{x'y'} = \overline{xy} - \overline{x}\,\overline{y},$$

here and hereafter prime denotes the deviation from the respective time mean. We use the term ''eddy flux'' for historical reason. As will be shown below, deviations from long-term means (e.g., x', y') contain variations not only on time scales of mesoscale eddies, but also on other time scales, such as the annual cycle and the near-inertial periods (see also Li and von Storch 2012, manuscript submitted to *J. Phys. Oceanogr*).

For the STORM/NCEP simulation, we stored monthly means of model values of all diagnostic parameters, including the accumulated two-variable-produces in all relevant combinations.[1] The results presented below are derived from the last decade (2001–10) of the STORM/NCEP simulation. In addition to monthly data, hourly output for January and July 2005 are used to assess the kinetic energy related to inertial gravity waves.

3. Terms of the LEC

The LEC describes the steady state balances of four energy reservoirs, the available potential energy P_m, and the kinetic energy K_m of the time-mean circulation (or for short the mean available potential energy and the mean kinetic energy), and the time-averaged available potential energy P_e and the kinetic energy K_e of the time-varying circulation (or for short the eddy available potential energy and the eddy kinetic energy). The derivation of the LEC in the ocean, in particular the four respective balances per unit volume, are provided in Appendix A. Here we limit ourselves to the LEC obtained by integrating the four balances over the entire ocean volume. Throughout this paper, we use capital letters to denote volume-integrated LEC-terms (except for some variables in the equations of motion, such as the surface heat flux H) and lower-case letters the respective LEC-terms per unit volume or unit area, or for any limited regions.

The mean available potential energy and the mean kinetic energy are defined as

$$P_m = -\int_V \frac{1}{2}\frac{g}{n_o}\overline{\rho}^{*2}\,dv, \quad \text{and} \tag{1}$$

$$K_m = \int_V \frac{1}{2}\rho_o(\overline{u}^2 + \overline{v}^2)\,dv, \tag{2}$$

and the eddy available potential energy and the eddy kinetic energy are defined as

[1] To reduce the output size, we stored our data in single precision that can distinguish 6 digits after comma. This way of storage is generally sufficient for most of the variables, except for the square of density, which is needed to calculate the eddy available potential energy. Because of extremely small variations in density, a large portion of the digits are used to store information that remains essentially unchanged, leaving very few digits to store the information about density variations.

$$P_e = -\int_V \frac{1}{2}\frac{g}{n_o}\overline{\rho^{*\prime 2}}\, dv, \quad \text{and} \tag{3}$$

$$K_e = \int_V \frac{1}{2}\rho_o \overline{(u'^2 + v'^2)}\, dv. \tag{4}$$

Here, n_o represents the vertical gradient of the time-mean and area-mean local potential density, and $\int_V dv$ indicates the integral over the ocean volume. Variable notation is standard and can be found in the appendix. The available potential energy of the time-mean circulation is determined by the square of the time mean of density anomalies ρ^* defined by

$$\rho^* = \rho - \rho_{\text{ref}}. \tag{5}$$

Here, ρ_{ref} is a predefined reference density. It is chosen to be the area average of the time-mean density $\langle\overline{\rho}\rangle$ and is a constant for a given level. The available potential energy of the time-varying circulation is determined by the variance of $\rho^{*\prime} = \rho^* - \overline{\rho^*}$.

In a steady state, P_m, P_e, K_m, and K_e satisfy,

$$\frac{dP_m}{dt} = C(P_e, P_m) - C(P_m, K_m) + G(P_m) - D(P_m) = 0, \tag{6}$$

$$\frac{dP_e}{dt} = -C(P_e, P_m) - C(P_e, K_e) + G(P_e) - D(P_e) = 0, \tag{7}$$

$$\frac{dK_m}{dt} = C(K_e, K_m) + C(P_m, K_m) + G(K_m) - D(K_m) = 0, \tag{8}$$

and

$$\frac{dK_e}{dt} = -C(K_e, K_m) + C(P_e, K_e) + G(K_e) - D(K_e) = 0, \tag{9}$$

where

$$G(P_m) = -\int_S g\frac{\alpha_{o,1}}{n_o}\overline{J}_s\overline{\rho^*}\, dS - \int_S g\frac{\beta_{o,1}}{n_o}\overline{G}_s\overline{\rho^*}\, dS, \tag{10}$$

$$G(P_e) = -\int_S g\frac{\alpha_{o,1}}{n_o}\overline{\rho' J'_s}\, dS - \int_S g\frac{\beta_{o,1}}{n_o}\overline{\rho' G'_s}\, dS, \tag{11}$$

$$G(K_m) = \int_S (\overline{\tau_{x,s}}\,\overline{u} + \overline{\tau_{y,s}}\,\overline{v})\, dS, \quad \text{and} \tag{12}$$

$$G(K_e) = \int_S (\overline{\tau'_{x,s}u'} + \overline{\tau'_{y,s}v'})\, dS, \tag{13}$$

are the rates of generation of P_m, P_e, K_m, and K_e, respectively. Here, $\tau_{x,s}$ and $\tau_{y,s}$ denote the stress exerted by the atmosphere on the ocean. Here, $\alpha_{o,1}$ and $\beta_{o,1}$ are values of expansion coefficients α_o and β_o in the upper most model layer. $J_s = (1/\rho_s c)H$ and $G_s = \overline{S}_1(E - P)$ are the temperature and salinity flux at the sea surface, where $c =$ 4000 J (kg K)$^{-1}$ is the specific heat of seawater and H the total heat flux at the sea surface, S_1 the time-mean salinity in the uppermost model layer, and E the evaporation rate and P the precipitation rate at the sea surface.

Denote the rate of conversion from X to Y by $C(X, Y)$. The rate of conversion from Y to X, $C(Y, X)$, equals $-C(X,Y)$. The four conversion rates in LEC are defined by

$$C(P_e, P_m) = -\int_V \frac{g}{n_o}\overline{\rho'\mathbf{u}'_h}\cdot\nabla_h\overline{\rho}\, dV, \tag{14}$$

$$C(K_e, K_m) = \int_V (\rho_o\overline{u'\mathbf{u}'}\cdot\nabla\overline{u} + \rho_o\overline{v'\mathbf{u}'}\cdot\nabla\overline{v})\, dV, \tag{15}$$

$$C(P_m, K_m) = -\int_V g\overline{\rho}\,\overline{w}\, dV, \quad \text{and} \tag{16}$$

$$C(P_e, K_e) = -\int_V g\overline{\rho' w'}\, dV. \tag{17}$$

Using the generation and conversion terms, the rates of dissipation $D(P_m)$, $D(P_e)$, $D(K_m)$, and $D(K_e)$ are derived as the residual from the respective balance equation.

It is noted that Eqs. (6)– (9) describe only the balances in a steady state. In particular, the rates of generation G, dissipation D, and conversion C in these equations ensure only that the time derivatives of K_m, K_e, P_m, and P_e vanish. They do not determine the steady state values of K_m, K_e, P_m, and P_e.

When considering the LEC, the question of how to define the available potential energy immediately arises. Here, we do not claim that we solve the problem of determining the ''availability.'' In fact, we did not tackle the complex question of how much of the potential energy is really available. Instead, we consider our LEC-formulation as a tool useful for studying the balances of and the transfers among the four energy compounds defined in Eqs. (1)–(4).

We note that Eqs. (6)–(9) are derived from various approximations (see appendix). In particular, the density equation [Eq. (A10) in appendix], from which the balance equations for the mean and eddy available potential energy are derived, is afflicted with additional approximations. One of them, formulated in Eq. (A7), states that the vertical gradient of the local potential density, which indicates the static stability, is constant temporally and horizontally and varies only with the

depth. This assumption can lead to notable errors in regions with weak stratification, since in the density budget, the vertical advection of the reference stratification (namely that related to n_o) is assumed to dominate the vertical advection of the perturbation. Apart from these assumptions and the errors induced by Eq. (A7), the LEC described above is well defined, meaning that all conversion terms from and to an available potential energy (e.g., either P_m or P_e) are not dependent of the choice of the reference density ρ_{ref}.

To see this, we note that there are three conversion terms that involve ρ^* and can hence, at least in principle, be dependent of ρ_{ref}. All of them occur in equations of the mean and eddy available potential energy per unit volume [Eq. (A13) and Eq. (A14) in appendix]. They describe, respectively, the conversion between eddy kinetic and eddy available potential energy, $g\overline{w'\rho^{*\prime}}$, the conversion between mean and eddy available potential energy, $(\partial g/\partial n_o)\overline{\rho^{*\prime}\mathbf{u}_h'}\cdot\nabla_h\overline{\rho}^*$, and the conversion between mean kinetic and mean available potential energy, $g\overline{w}\,\overline{\rho}^*$. The first two conversions are independent of ρ_{ref}, since for a spatially constant ρ_{ref}, $\nabla_h\overline{\rho}^* = \nabla_h\overline{\rho}$, and since

$$\rho^{*\prime} = (\rho - \rho_{\text{ref}}) - \overline{\rho - \rho_{\text{ref}}} = \rho - \overline{\rho} = \rho' \tag{18}$$

so that

$$\overline{\rho^{*\prime}\mathbf{u}_h'} = \overline{\rho'\mathbf{u}_h'}, \quad \overline{w'\rho^{*\prime}} = \overline{w'\rho'}. \tag{19}$$

The situation is somewhat different for the last conversion. Generally, one has $g\overline{w}\,\overline{\rho}^* \neq g\overline{w}\,\overline{\rho}$ and $g\overline{w}\,\overline{\rho}_1^* \neq g\overline{w}\,\overline{\rho}_2^*$, where ρ_1^* and ρ_2^* are deviations from two different reference densities. Thus, *when considering a unit volume*, the conversion between the mean kinetic and the mean available potential energy depends on the reference density. When applying global volume integral, on the other hand, one finds

$$\int_V \overline{w}\,\overline{\rho}^*\,dv = \int_V \overline{w}(\overline{\rho} - \rho_{\text{ref}})\,dv = \int_V \overline{w}\,\overline{\rho}\,dv.$$

This is because $\int_V \overline{w}\rho_{\text{ref}}\,dv$ equals $\rho_{\text{ref}}\int_V \overline{w}\,dv$ and $\int_V \overline{w}\,dv$ vanishes at each time step in MPI-OM in which the flows are nondivergent and satisfy no-normal-flow condition at the boundaries. In fact, not only the volume but also the area integral of w vanishes. Thus, *when integrated globally*, the conversion between the mean kinetic and the mean available potential energy, $C(P_m, K_m)$, is independent of ρ_{ref}.

Not only the conversion terms, the generation of the eddy available potential energy, which involves $\overline{\rho^{*\prime}J'}$ and $\overline{\rho^{*\prime}G'}$, is also independent of ρ_{ref}, since Eq. (18) implies

$$\overline{\rho^{*\prime}J'} = \overline{\rho'J'}, \quad \overline{\rho^{*\prime}G'} = \overline{\rho'G'}. \tag{20}$$

For the same reason, the eddy available potential energy, which is proportional to $\overline{\rho^{*\prime 2}} = \overline{\rho'^2}$, is also independent of ρ_{ref}.

Apart from P_m itself, the only term that depends on ρ_{ref} is the generation of the mean available potential energy via the mean heat and buoyancy flux at the sea surface defined in Eq. (10). Because of the spatial variations of the expansion coefficients, in particular those of $\alpha_{o,1}$, $G(P_m)$ depends on the choice of ρ_{ref}, even when ρ_{ref} is a constant and the area integrals of H and $E - P$ vanish for an ocean that is in its steady state.

In summary, three out of the four energy reservoirs, namely P_e, K_m, and K_e, are by definition almost independent of ρ_{ref}, and all G and C terms, except for the generation rate of the mean available potential energy $G(P_m)$, are by definition independent of the choice of ρ_{ref}. It will be shown in section 5 that the value of $G(P_m)$ varies not too much for a reasonable range of ρ_{ref}.

4. Energy reservoirs

The four reservoirs are calculated following Eqs. (1)–(4). The kinetic energy of the time-mean and time-varying circulation, K_m and K_e, are well defined and can be accurately estimated. K_m amounts to 1.27 EJ (exajoules = 10^{18} joules). Figure 1 and Fig. 2 show the horizontal distributions of $0.5(\overline{u}^2 + \overline{v}^2)$ and $0.5(\overline{u'^2} + \overline{v'^2})$ at 100- and 2038-m depth. For the time-mean circulation (Fig. 1a and Fig. 2a), strong kinetic energies are concentrated in sharp equatorial currents, sharp boundary currents, and narrow filaments in the Southern Ocean that form the ACCs. Most of the narrow filaments are along the zonal direction and indicate narrow zonal jets, consistent with the satellite altimetry data (Maximenko et al. 2005; Scharffenberg and Stammer 2010). The amplitude of the equatorial currents reaches about 1 m s^{-1} at 100 m. The sharp currents in the Gulf Stream region reach about 1 m s^{-1} in the upper ocean. The velocity maxima in the filaments in the Southern Ocean are about 20 cm s^{-1} at 2000 m. Note that the strength of the ACC varies notably as it flows eastward, and that the time-mean kinetic energy in the deep ocean is almost exclusively concentrated in the Southern Ocean. It is striking how little the paths of these currents vary over time so that regions of strong and weak currents, characterized by differences in $0.5(\overline{u}^2 + \overline{v}^2)$ that are larger than one order of magnitude, can exist side by side during the time-average period of 10 years and result in narrow fine structures in Fig. 1a and Fig. 2a.

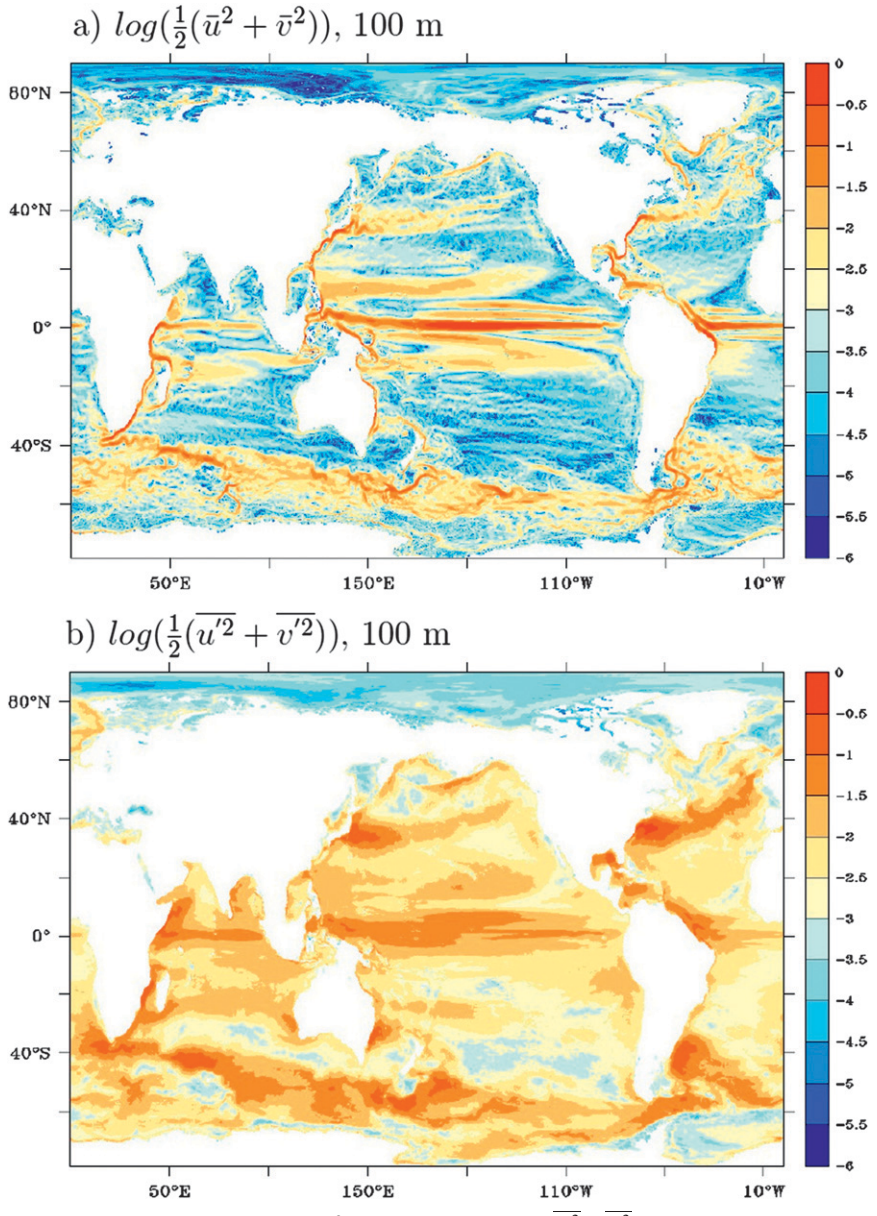

FIG. 1. Distribution of (a) $\log[0.5(\bar{u}^2 + \bar{v}^2)]$ and (b) $\log[0.5(\overline{u'^2} + \overline{v'^2})]$ at 100-m depth derived from the decade 2001–10 of the STORM simulation ($m^2\ s^{-2}$).

The mean kinetic energy of the time-varying circulation K_e is almost three times stronger than that of the time-mean circulation and reaches 3.55 EJ. It should be noted that K_e represents, by construction, kinetic energy related to variations on time scales ranging from the model time step of 600 s to the analysis period of 10 years. Thus, not only mesoscale eddies but also other features such as the annual cycle and inertial waves contribute to K_e.

The horizontal distributions of $0.5(\overline{u'^2} + \overline{v'^2})$ (Fig. 1b and Fig. 2b) show that the time-varying circulation is much more energetic and its related kinetic energy reveals, when averaged over time, much smoother spatial structures than the time-mean circulation (Fig. 1a and Fig. 2a). The smoothness indicates a large variability in the positions of the mesoscale eddies and other transient features captured in $0.5(\overline{u'^2} + \overline{v'^2})$. The maxima of $0.5(\overline{u'^2} + \overline{v'^2})$ are located near, but not always in the sharp currents. For instance in the North Atlantic and North Pacific, the largest values of $0.5(\overline{u'^2} + \overline{v'^2})$ are spread out downstream away from the coasts, whereas the largest values of $0.5(\bar{u}^2 + \bar{v}^2)$ are confined within narrow strips along the coasts. Generally, eddy kinetic energy is often higher in regions with weak mean

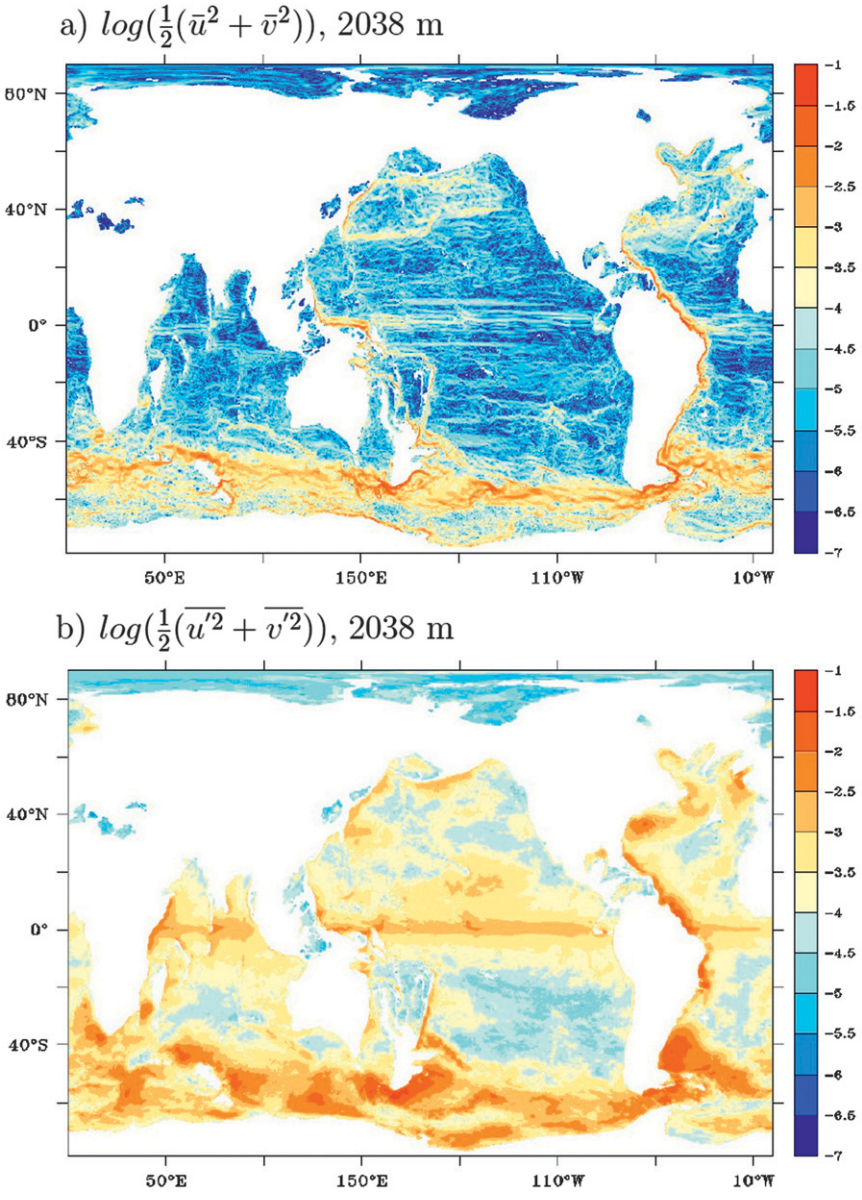

FIG. 2. Distribution of (a) $\log[0.5(\bar{u}^2 + \bar{v}^2)]$ and (b) $\log[0.5(\overline{u'^2} + \overline{v'^2})]$ at 2038-m depth derived from the decade 2001–10 of the STORM simulation ($m^2\ s^{-2}$).

circulation. To demonstrate this, Fig. 3a shows the ratio of $0.5(\overline{u'^2} + \overline{v'^2})$ to $0.5(\bar{u}^2 + \bar{v}^2)$ at 100 m. Within sharp topographically controlled boundary currents, in the equatorial Pacific and Atlantic, and within the filaments of the ACC, the eddy kinetic energy is weaker than the mean kinetic energy. Outside strong currents, in particular in the subtropical and midlatitude regions where the values of $0.5(\overline{u'^2} + \overline{v'^2})$ are smaller than 10^{-3} $m^2\ s^{-2}$, the eddy kinetic energy is up to one to two orders of magnitude larger than the mean kinetic energy. This relation between the mean and the eddy kinetic energy are consistent with the satellite altimetry data (Scharffenberg and Stammer 2010). The same relation exists also in the deep ocean (not shown).

The vertical profiles of area-averages of $0.5(\overline{u'^2} + \overline{v'^2})$ and $0.5(\bar{u}^2 + \bar{v}^2)$ reveal that kinetic energy decreases drastically with increasing depth and the intensity of the time-varying circulation is stronger than that of the time-mean circulation throughout the water column (Fig. 4). Translated into velocity speed, one has for the time-varying circulation an area-averaged value of about 28 cm s^{-1} in the first model layer and about 3 to 4 cm s^{-1} below about 3 km. The respective values for the time-mean circulation are up to 50% smaller.

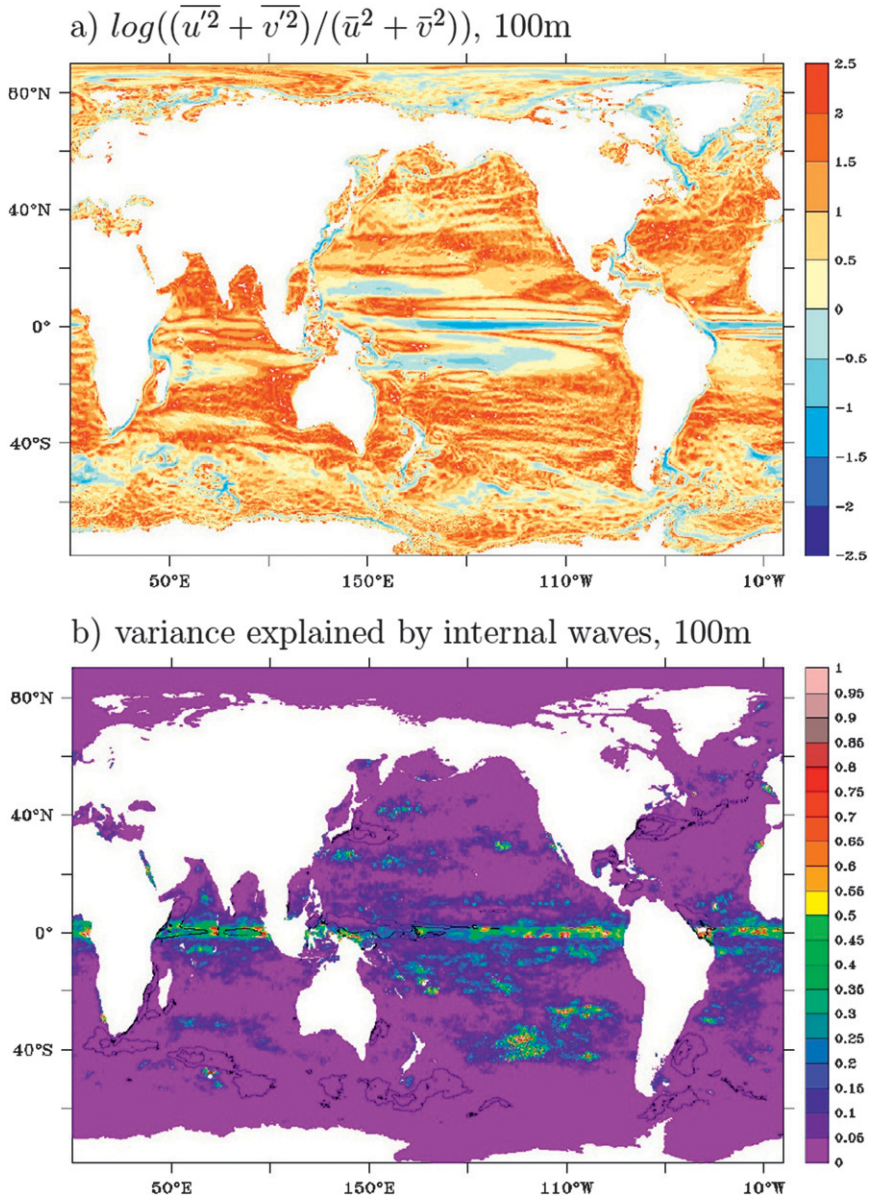

FIG. 3. Ratios of (a) $0.5(\overline{u'^2} + \overline{v'^2})$ to $0.5(\bar{u}^2 + \bar{v}^2)$ and of (b) the high-pass-filtered k_e to total k_e at 100-m depth. Logarithm is used for the first ratio. The high-pass-filtered k_e is derived by filtering out variations at frequencies lower than f using hourly data for January and July 2005. Also shown in (b) are isolines of $0.5(\overline{u'^2} + \overline{v'^2})$, ranging from 0.025 to 0.15 $m^2\ s^{-2}$ with an isoline interval of 0.025 $m^2\ s^{-2}$.

Being driven by 6 hourly winds from the NCEP–NCAR reanalysis, the MPI-OM/TP6ML80 model produces strong near-inertial waves. To get some idea about how much of the velocity variations originate from variations at frequencies higher than the inertial frequency f, we carried out Fourier decompositions at each grid point for hourly velocities in January and July 2005 of the STORM/NCEP simulation, and integrated the spectral estimates over frequencies larger than f. In this way, we obtained an estimate of variances related to the simulated internal waves, including inertial oscillations. Outside an equatorial band of, about ±5°, the inertial periods are shorter than 6 days, and are therefore reasonably well resolved by hourly velocities over a period of one month. Figure 3b shows the high-pass-filtered variance relative to the total variance. In these non-equatorial regions, variances at frequencies larger than f account up to 20%–40% or more of the total velocity

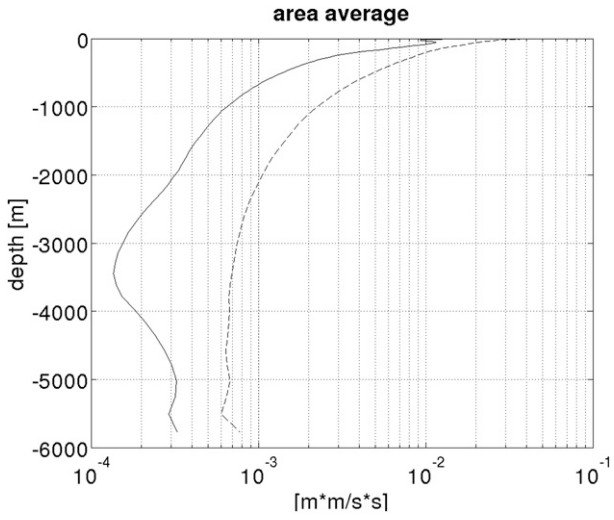

FIG. 4. Vertical profiles of area averages of $0.5(\overline{u}^2 + \overline{v}^2)$ (solid) and $0.5(\overline{u'^2} + \overline{v'^2})$ (dashed) as a function of depth.

variances in a substantial part of the tropical and subtropical oceans. These high-frequency variations are especially strong in the tropical and subtropical South Pacific, but contribute little to the total variances in regions with large values of $0.5(\overline{u'^2} + \overline{v'^2})$, highlighted by black lines in Fig. 3b. There, more than 95% of the total variance originate from variations at frequencies lower than the inertial frequency f. In other words, k_e results mainly from mesoscale eddies. Integrated globally, variations at frequencies higher than f account for 0.4 EJ, which is roughly 10% of K_e. For comparison, the estimate of the kinetic energy of inertial waves given by Ferrari and Wunsch (2010) is 0.7 EJ.

The two other energy reservoirs of the LEC, the available potential energy of the time-mean and time-varying circulation, P_m and P_e, have different relations to the choice of the reference density. Here, P_m is strongly affected by the choice of the reference density ρ_{ref}. Consequently, the global value of 166 ZJ (zettajoules = 10^{21} joules) is not particularly meaningful. On the other hand, P_e does not depend on ρ_{ref}, provided that the errors arising from Eq. (A7) can be neglected. It amounts to 6.38 EJ. However, P_e is not well estimated because of the reduced precision of the stored data. When integrated $\overline{\rho'^2}$ over each model layer, we obtain a vertical profile that has large positive values (as it should be the case by definition) in the upper few hundred meters and small values with alternating signs below 1000 m. It seems that the magnitude of $\overline{\rho'^2}$ is noticeably larger than that of the rounding errors in the upper ocean, but comparable to the size of rounding errors below 1000 m. The large positive values indicate that the order of P_e is likely correctly derived from the simulation, but the spatial distribution of $\overline{\rho'^2}$, in particular that in the deep ocean, should be considered with caution.

5. Generation of kinetic and available potential energies

The power supplied by the time-mean winds to the time-mean circulation, $G(K_m)$, amounts to 1.85 TW (terawatts = 10^{12} watts) and that supplied by the time-varying winds to the time-varying circulation, $G(K_e)$, amounts to 2.19 TW. The two numbers are comparable to $G(K_m) = 1.98$ TW and $G(K_e) = 1.79$ TW that were derived from the simulation with the OGCM For the Earth Simulator (OFES) (von Storch et al. 2007). That the value of $G(K_m)$ is about 7% lower in the STORM/NCEP simulation than in the OFES simulation can be caused, at least partially, by the fact that the former is based on averages obtained over 10 years, whereas the latter is obtained from averages over 5 years only. By using a shorter averaging period, some of the long-term variability might not be averaged out and can reside in the time-means, leading to somewhat larger value of $G(K_m)$. The value of $G(K_e)$ is about 18% higher in the STORM/NCEP simulation than in the OFES simulation. This difference can be a direct consequence of calculating $\overline{\tau'_x u'}$ and $\overline{\tau'_y v'}$ using accumulated products $\overline{\tau_x u}$ and $\overline{\tau_y v}$, rather than snapshots sampled every three days. Certainly, the differences can also be caused by the different models used. Of the total generation of 2.19 TW through the time-varying winds in STORM/NCEP, 0.27 TW, or about 12%, is caused by the mean annual cycle in the winds. This value compares also well with the respective value (0.29 TW) obtained from the OFES simulation. Overall, the amount of wind-supplied power obtained from the STORM/NCEP run is comparable to that found in the OFES simulation based on a different OGCM. It should be noted that the numbers provided here represent wind input to the circulation (not to the surface waves).

Apart from the differences in the magnitude, the geographic distributions of the respective generation terms per unit volume (Figs. 5a,b) resemble those obtained from the OFES simulation. This is particularly true concerning the following two aspects. First, the power input from the time-mean wind stresses is most intense in the Southern Ocean (see both the two-dimensional distribution and the meridional profile in Fig. 5a), as it is also found in the Ocean Topography Experiment (TOPEX) altimeter data (Wunsch 1998). In both the STORM/NCEP and the OFES simulation, the generation from the time-mean wind stress is larger south of Africa and in the Indian Ocean sector of the

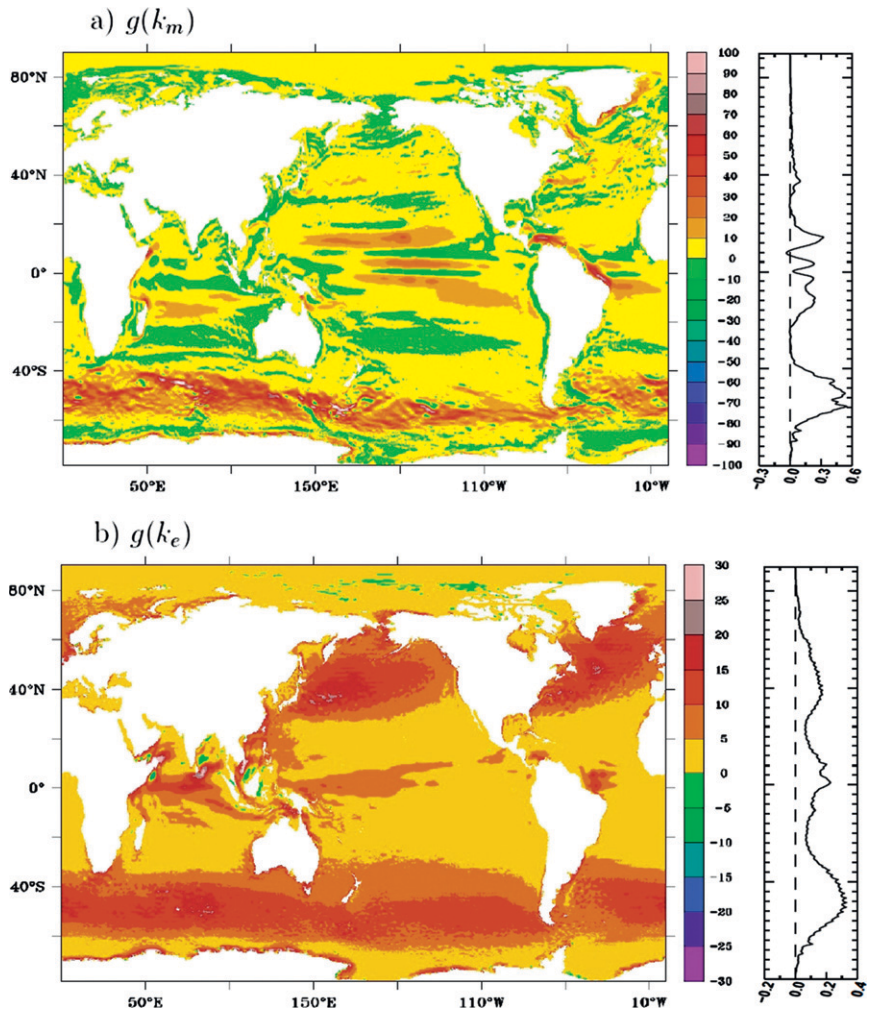

FIG. 5. Horizontal distributions of (top) the power input to the time-mean circulation via time-mean winds $g(k_m)$ and (bottom) the power input to the time-varying circulation via the time-varying winds $g(k_e)$ in 10^{-3} W m^{-2}. The right profiles show the zonal integrals of the respective quantities in 10^6 W m^{-1}.

Southern Ocean than those farther eastward. This east–west asymmetry is also evident in Wunsch's estimate. It should be noted that the generation from the time-mean wind stress in Wunsch's estimate are smaller than those shown in Fig. 5a, since Wunsch (1998) considered the power input from the mean winds to the geostrophic circulation below the main Ekman layer, rather than the total power input from the time-mean winds at the sea surface. Second, the power input from the time-varying wind stress is positive almost everywhere (Fig. 5b), meaning that the time-varying current velocity is, on average, orientated in the same direction as the time-varying wind stress. Note that the pattern of $g(k_e)$ differs notably from that of the eddy kinetic energy in Fig. 1b.

The surface buoyancy flux can generate density differences and variances, and from that the mean and eddy available potential energy, by heating relatively light water masses and by adding freshwater to relatively light water masses, and by cooling relatively heavy water masses and by extracting freshwater from relatively heavy water masses. Figure 6 and Fig. 7 show the generation via the heat flux and freshwater flux, respectively. In Fig. 6a and Fig. 7a, ρ^* is calculated as the deviation from the time-mean area-mean surface density $\langle\overline{\rho}\rangle$.

Regarding the time-mean density differences, the net generation rate of 2.00 TW is composed of a contribution of 1.87 TW from the mean heat flux and a contribution of 0.13 TW from the mean fresh-water flux ($E - P$). The contribution from heat flux results mainly from two factors, 1) the constant loss of heat in polar regions, which maintains the density of the heavy water masses there

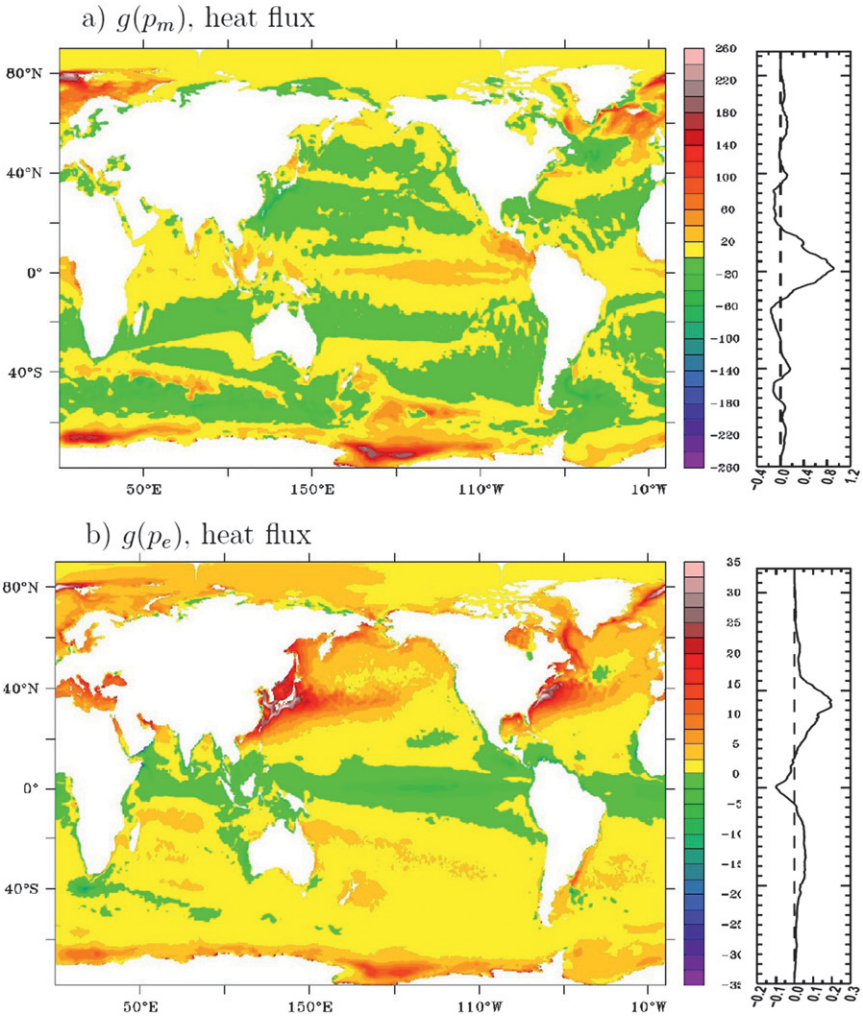

FIG. 6. As in Fig. 5, also in the same units, but for the generation rate of the available potential energy via (top) the time-mean and by (bottom) the time-varying heat fluxes. Coefficients α_o, β_o, and n_o are derived from the annual mean temperature and salinity averaged over the decade 2001–10.

against diffusion and reaches magnitudes of more than 100 mW m^{-2} (1 mW = 10^{-3} W), and 2) the constant gain of heat in the tropical regions, which maintains the density of light water masses against diffusion there and reaches magnitudes of about 20–40 mW m^{-2} (Fig. 6a). The contribution from freshwater flux results mainly from constantly adding freshwater (excess precipitation over evaporation) into lighter water masses in the tropics, with the maximum generation rate reaching about 20 mW m^{-2} (Fig. 7a). On the other hand, both the heat flux and the freshwater flux can also remove density differences. Removal via heat flux occurs in most of the subtropical and midlatitude regions, with the generation rate being stronger than 40 mW m^{-2} in the Kuroshio and Gulf Stream regions, where heat is lost from warmer and lighter water masses. The removal via the freshwater flux occurs in the high-latitude regions, where precipitation is in excess of evaporation over water masses that are denser than those in the tropics. Overall the generation of density difference outweighs the removal of density difference, and the freshwater flux is much less efficient in changing density than the heat flux.

The generation of variances of time-varying density anomalies is determined by the correlation of buoyancy flux with density anomalies. The magnitude of the generation via time-varying heat flux (Fig. 6b) is comparable or even larger than that via the time-mean freshwater flux (Fig. 7a). The generation via the time-varying freshwater flux (Fig. 7b) is about one order

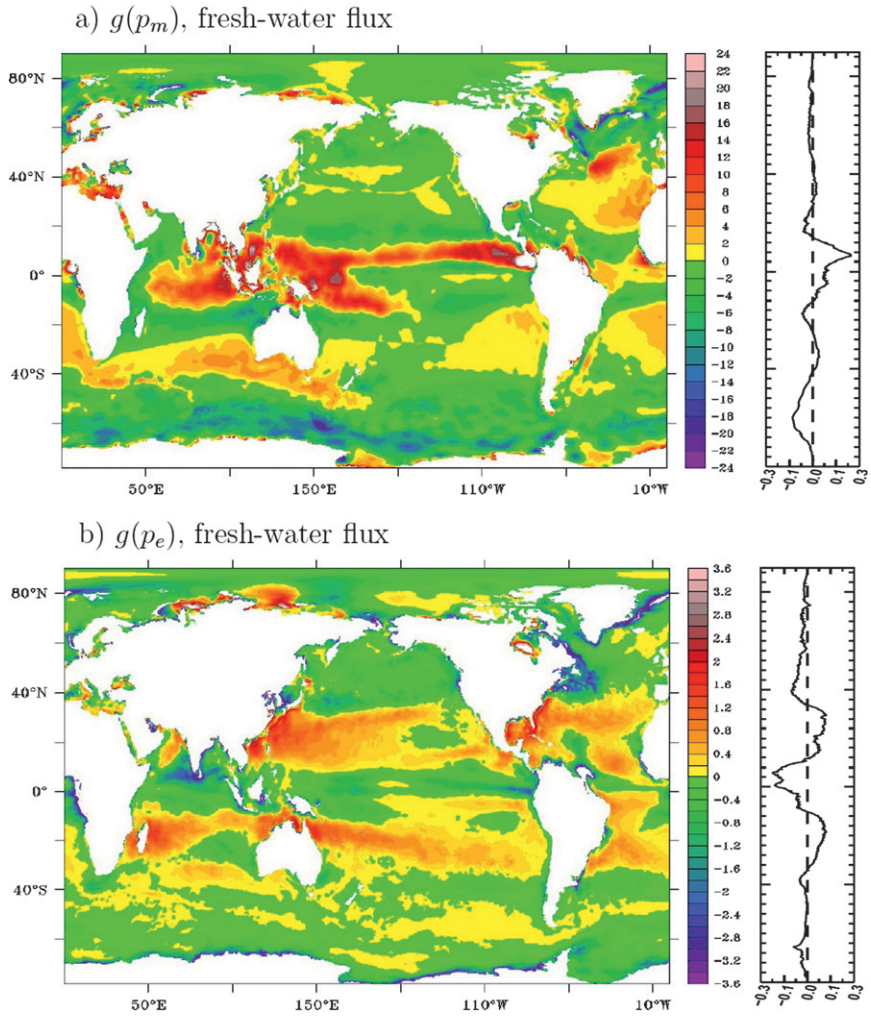

FIG. 7. As in Fig. 6, also in the same units, but for the generation rate of the available potential energy via (top) the time-mean and by (bottom) the time-varying fresh-water fluxes.

of magnitude smaller than the generation via the time-mean freshwater flux. The generation via time-varying heat flux is positive over most of the extratropical regions, with maximum generation rate of about 30 mW m^{-2} in the Kuroshio and Gulf Stream regions. This is partially due to the fact that the turbulent heat fluxes are directly coupled to the sea surface temperatures.

To have some idea about how $G(P_m)$ varies with the choice of the reference density, we recalculated $G(P_m)$ by changing ρ_{ref} to $\langle\overline{\rho}\rangle \pm 1$ kg m^{-3}. The overall structures as seen in Fig. 6a and Fig. 7a remain essentially the same, but the relative magnitudes of positive and negative values are different, resulting in different values of $G(P_m)$ (Table 1). The differences are about 20%. Thus, if we assume that the reference density should not be too different from $\langle\overline{\rho}\rangle$, we would accept that the order of magnitude of $G(P_m)$ is reasonably estimated. In the following, we assume that the dependence of $G(P_m)$ on ρ_{ref} is weak.

6. Exchanges between the four energy reservoirs

This section discusses conversion terms, $C(X, Y)$ or $c(x, y)$. Positive values of $C(X, Y)$ or $c(x, y)$ indicate that X or x is converted into Y or y, whereas negative values of $C(X, Y)$ or $c(x, y)$ indicate that Y or y is converted into X or x, consistent with the notion $C(X, Y) = -C(Y, X)$ or $c(x, y) = -c(y, x)$.

a. Conversion between mean and eddy available potential energy

According to Eq. (14), eddy available potential energy will be converted into mean available potential energy when the eddy density flux $\overline{\rho'\mathbf{u}_h'}$ is in the direction of the

TABLE 1. The rate of generation of the mean available potential energy P_m due to heat flux $G(P_m)_H$, evaporation minus precipitation $G(P_m)_{E-P}$, and both $G(P_m)$. Three different reference densities are used. $\langle\overline{\rho}\rangle = 1024.3$ kg m^{-3} indicates the time-mean and area-mean surface density.

	$\langle\overline{\rho}\rangle + 1\,\mathrm{kg\,m^{-3}}$	$\langle\overline{\rho}\rangle$	$\langle\overline{\rho}\rangle - 1\,\mathrm{kg\,m^{-3}}$
$G(P_m)_H$	2.25	1.87	1.49
$G(P_m)_{E-P}$	0.09	0.13	0.16
$G(P_m)$	2.34	2.00	1.65

mean density gradient. In the upper ocean, the eddy density flux $\overline{\rho'v'}$, which is predominantly poleward within the tropical band of ±20° and equatorward north and south of this band, is mostly directed opposing the model-meridional gradient of the mean density $\partial\overline{\rho}/\partial y$ (not shown). The relation between the zonal eddy density flux $\overline{\rho'u'}$ and the model-zonal gradient of the mean density $\partial\overline{\rho}/\partial x$ is much less systematic. As a result, most of the negative values of $c(p_e, p_m)$ in the model upper ocean, which indicate conversions from p_m to p_e, result from the down-gradient meridional eddy density flux. The largest conversion from p_m to p_e occurs in the upper ocean in the equatorial region and in the Gulf Stream and Kuroshio regions. The magnitude of $c(p_e, p_m)$ decreases with increasing depth. The conversion remains being directed from the mean available potential energy to the eddy available potential energy in the deep ocean and is strongest in the Southern Ocean, mostly due to the down-gradient meridional eddy density flux there. When integrated vertically (Fig. 8), the values of $c(p_e, p_m)$ are mostly negative. The meridional profile of the vertical integral (right profile in Fig. 8) reveals maxima near 35°N, just north of the equator and around 40°–50°S. Integrated over the entire ocean, the total conversion is directed from P_m to P_e and amounts to 0.83 TW.

b. Conversion between eddy available potential energy and eddy kinetic energy

The conversion between the eddy kinetic and eddy available potential energy [Eq. (17)] is determined by the covariance between density and vertical velocity. Positive values of $c(p_e, k_e)$ are obtained when denser water masses correlate with downward movements and lighter water masses correlate with upward movements. They indicate conversions from eddy available potential energy to eddy kinetic energy and measure the strength of the baroclinic production.

The geographical distributions of positive $c(p_e, k_e)$ suggest that baroclinicity prevails in most of extratropical regions at 100 m and essentially only in the Southern Ocean at about 2000 m (not shown). Figure 9 shows the distribution of vertically integrated $c(p_e, k_e)$. A comparison with the distributions of k_e suggests that to a first approximation, there is a good agreement between eddy activity, as indicated by large values of k_e in Fig. 1b and Fig. 2b, and baroclinic production, as indicated by large positive values of $c(p_e, k_e)$ in Fig. 9, in most of the extratropical oceans. However, not all strong velocity variations are related to baroclinicity. This is particularly true for the tropical variations in the upper ocean that result, amongst others, from tropical instability waves (see, e.g., Jochum et al. 2004). For these variations, $c(p_e, k_e)$ has mostly negative values, indicating

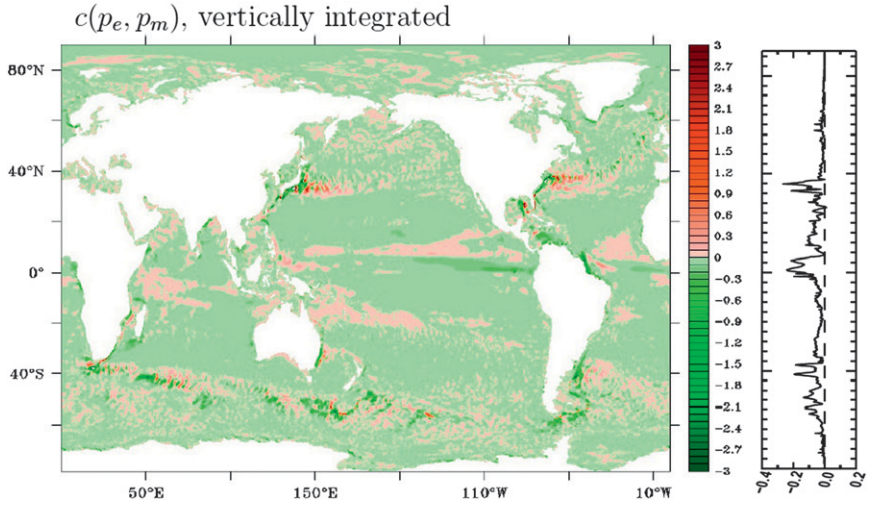

FIG. 8. Horizontal distribution of the vertically integrated rate of conversion from eddy to mean available potential energy [$c(p_e, p_m)$; 10^{-1} W m^{-2}]. The right profile shows the zonal integrals of this vertically integrated conversion (10^6 W m^{-1}).

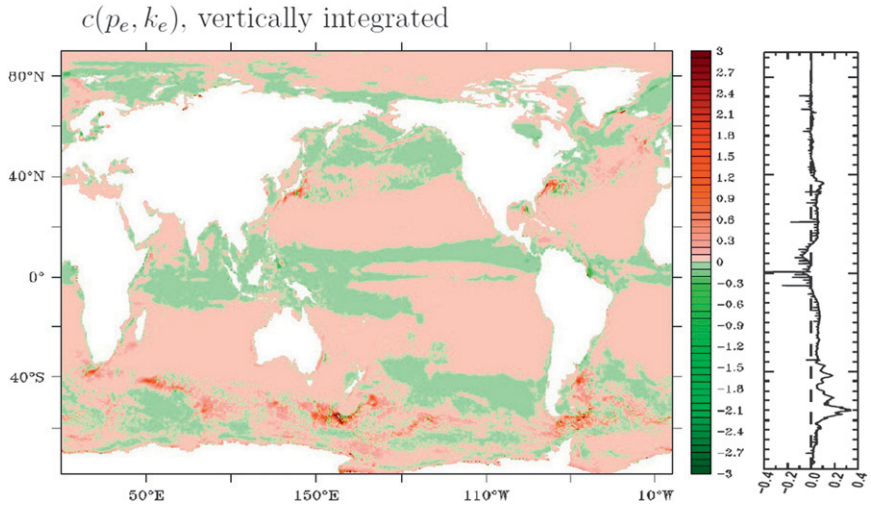

FIG. 9. As in Fig. 8, but for the vertically integrated rate of conversion from eddy available potential energy to eddy kinetic energy, $c(p_e, k_e)$.

conversions from eddy kinetic energy to eddy available potential energy. There are also other places where maxima in k_e do not correspond to positive values of $c(p_e, k_e)$. For instance, large values in k_e are found along the western boundaries of the tropical Atlantic and the South Atlantic at about 2000 m (Fig. 2b), where $c(p_e, k_e)$ is mostly small or even negative, suggesting that mechanisms other than baroclinic instability must be responsible for the generation of k_e there.

The vertical profile of area integrated $c(p_e, k_e)$ reveals positive values at all depths (not shown). Thus, eddy available potential energy is converted to eddy kinetic energy throughout the water column. This conversion has nearly constant strength in the upper 1500 m, and decreases drastically with increasing depth below 2000 m. The weak dependence on depth in the upper 2 km results from a decrease in baroclinic production with depth in the Gulf Stream and Kuroshio and an increase in baroclinic production with depth in the Southern Ocean. Integrated over the entire ocean, the conversion from eddy available potential energy to eddy kinetic energy amounts to 0.73 TW.

c. *Conversion between eddy kinetic energy and mean kinetic energy*

The vertical profile of $c(k_e, k_m)$ integrated over each model layer shows negative values above about 2.5 km and positive values below about 2.5 km (Fig. 11a). Thus, eddy kinetic energy is converted to mean kinetic energy only in the deep ocean. In the upper 2.5 km, the conversion goes the other way around. The negative values of $c(k_e, k_m)$ in the upper ocean are located mainly in the tropical and subtropical oceans, but also in the midlatitude regions around 40°N and 40°S (Fig. 10a). When decomposing $c(k_e, k_m)$ into the term related to horizontal gradients of the mean zonal velocity $\rho_o \overline{u'\mathbf{u}_h'} \cdot \nabla_h \overline{u}$ and the term related to the horizontal gradients of the mean meridional velocity $\rho_o \overline{v'\mathbf{u}_h'} \cdot \nabla_h \overline{v}$, we find that the former makes a larger contribution to negative $c(k_e, k_m)$ in the upper ocean than the latter, indicating the dominant role of shear instability related to the mean zonal flows in the upper tropical oceans, resulting in phenomena such as tropical instability waves (Jochum et al. 2004). In the deep ocean, large values of both signs are found in the Southern Ocean (left plot in Fig. 10b). When zonally integrated (right plot in Fig. 10b), we find a large conversion from k_e to k_m around 55°S.

We further investigated the role of the Southern Ocean by integrating $c(k_e, k_m)$ over 40°–65°S for each model layer. Figure 11b shows that when integrated over the Southern Ocean (40°–65°S) for each model layer, the net conversion is from mean kinetic energy to eddy kinetic energy in the upper 3000 m and the other way around further below. Given the fact that the strongest power input with maxima reaching about 50 mW m^{-2} comes from the time-mean winds to the time-mean circulation in the Southern Ocean (Fig. 5a), the net conversion from mean kinetic energy to eddy kinetic energy in the Southern Ocean indicates a power pathway from winds to the time-mean circulation and eventually to the time-varying circulation, at least in the upper ocean.

d. *Conversion between mean kinetic energy and mean available potential energy*

As pointed out in section 3, only the area integral of $c(p_m, k_m)$ is independent of the choice of ρ_{ref} that is used to define the mean available potential energy. Because of that, we consider only the vertical profile of the area

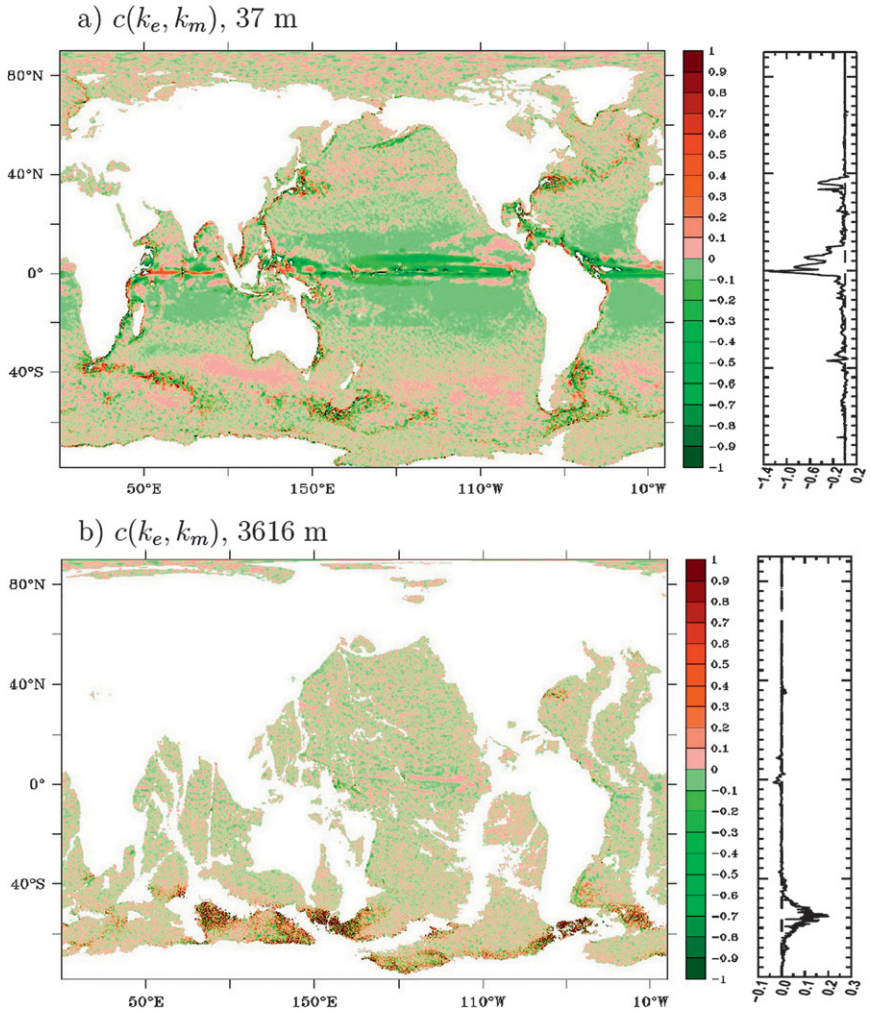

FIG. 10. Horizontal distributions of the conversion $c(k_e, k_m)$ at (top) 37 m and (bottom) 3616 m (10^{-4} and 10^{-5} W m^{-3}, respectively). The right profiles show the zonal integrals of the respective quantities (10^3 W m^{-2}).

integral of the conversion between p_m and k_m. Since the area integral of $\overline{w}$ vanishes, the area integrals will only be nonzero, when the density of water masses that are transported upward differs from the density of water masses that are transported downward. The resulting profile (Fig. 12) shows that the mean kinetic energy is converted into the mean available potential energy in the upper 3 km, whereas the opposite is the case below 3 km. Integrated over the entire ocean volume, the conversion rate amounts to 0.49 TW and is directed from mean kinetic energy into mean available potential energy.

7. Dissipation of kinetic and available potential energies

The rates of dissipation are diagnosed from the rates of generation and conversion discussed in the previous sections, as residuals of the balances given in Eqs. (6)–(9). The net dissipation amounts to 6.7 TW. About one-third of this dissipation results from the dissipation of the available potential energy, which is to a large extent but not exclusively, due to the harmonic diffusion used in the STORM/NCEP model that tends to smooth out isopycnical density differences. The other two-thirds, which result from the dissipation of kinetic energy and are affected by the biharmonic viscosity used in the model, are directly related to the power input from the winds. From these two-thirds of the net dissipation, 1.4 TW are used to dissipate the mean kinetic energy and 3 TW are used to dissipate the eddy kinetic energy. In the discussion of the general circulation of the ocean, the power required to maintain the stratified quasi-steady state of the deep ocean is estimated to be of the order of 2 TW (Munk and Wunsch 1998; Wunsch and Ferrari

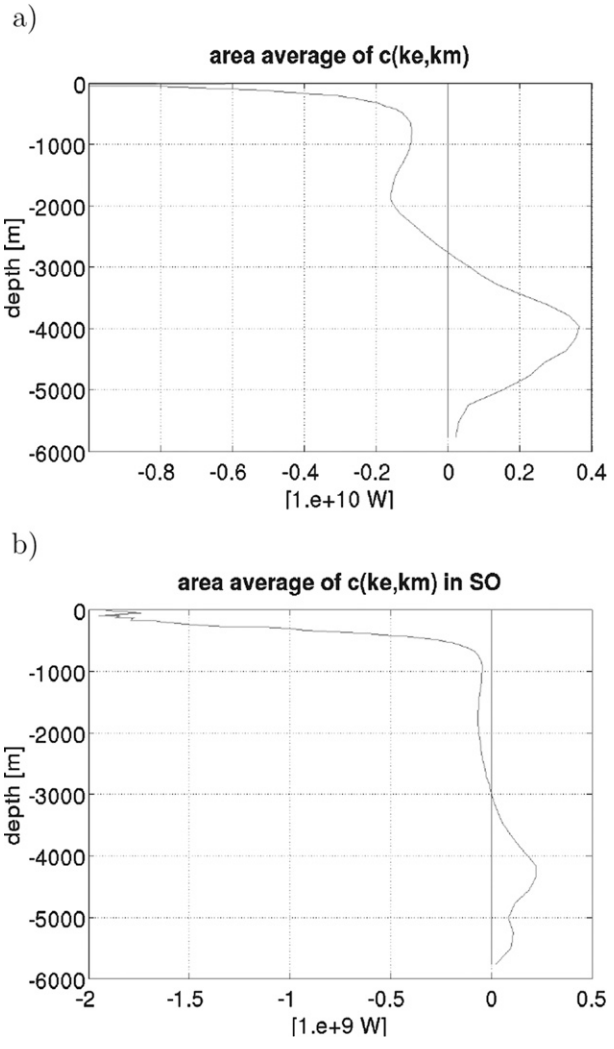

FIG. 11. (a) Vertical profile of area integrals of the conversion rate from the eddy kinetic energy to the mean kinetic energy (10^{10} W), and (b) vertical profile of the same quantity but integrated over the area in the Southern Ocean from 40° to 65°S (10^{9} W).

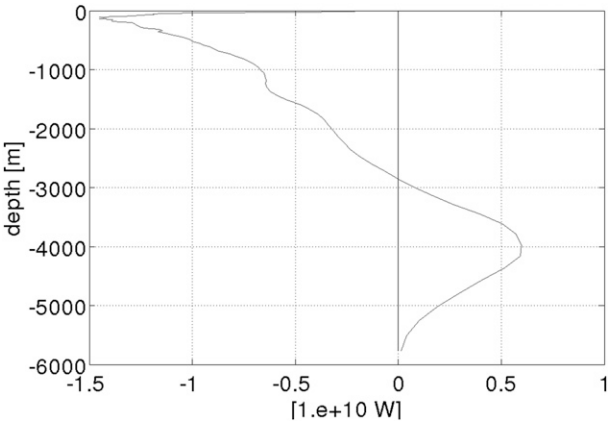

FIG. 12. Vertical profile of area integrals of the conversion from the mean available potential energy to the mean kinetic energy (10^{10} W).

2004). It is thought that half of this power comes from the tides and the other half from the winds. One way to turn the wind input at the surface into mechanical power for mixing in the oceanic interior is that via breaking of internal waves emitted by eddying flows. The 3 TW that result mainly from the dissipation of mesoscale eddies suggest that, if eddying flows are capable of emitting internal waves, notable amount power can be passed from mesoscale eddies to internal waves.

8. The oceanic LEC

One goal of the present study is to understand, in a more quantitative way and under the assumption that the MPI-OM/TP6ML80 is able to represent the oceanic LEC realistically, how the ocean general circulation functions. One way to achieve this goal is by comparing the estimated oceanic LEC with the LEC of the atmosphere. The oceanic LEC is summarized in Fig. 13a. An estimate of the atmospheric LEC is shown in Fig. 13b, where the values of Li et al. (2007), as derived from the 40-yr ECMWF Re-Analysis (ERA-40), are transformed into the same units as in Fig. 13a. Figure 13b suggests a dominant power pathway $P_m \rightarrow P_e \rightarrow K_e$ and a weak continuation to K_m, with $C(P_m, P_e)$ and $C(P_e, K_e)$ being the largest conversions within the atmospheric LEC and having the same order of magnitude, and a clear conversion from K_e to K_m, with $|C(K_e, K_m)|$ being notably smaller than $|C(P_m, P_e)|$ and $|C(P_e, K_e)|$, but much larger than $|C(P_m, K_m)|$ These features are also found in other estimates, including both the older estimates (Peixoto and Oort 1992) and those obtained from different climate models (Hernández Deckers and von Storch 2010; Hernández Deckers and von Storch 2011). Less certain is the conversion $C(P_m, K_m)$, which is not always positive, though always about one order of magnitude smaller than $C(P_m, P_e)$ and $C(P_e, K_e)$ in all previous estimates. In the following comparison, we will assume that the total conversion from P_m to K_m in the atmosphere is much weaker than the other three conversions.

Regarding energy reservoirs, the mean available potential energy P_m is much larger than the other three reservoirs in the ocean. Because of its dependence on the choice of the reference density, P_m is not particularly meaningful and will hence not be discussed further. Apart from P_m, the oceanic circulation is much less energetic than the atmospheric circulation with the reservoirs P_e, K_e, and K_m in Fig. 13a being about two

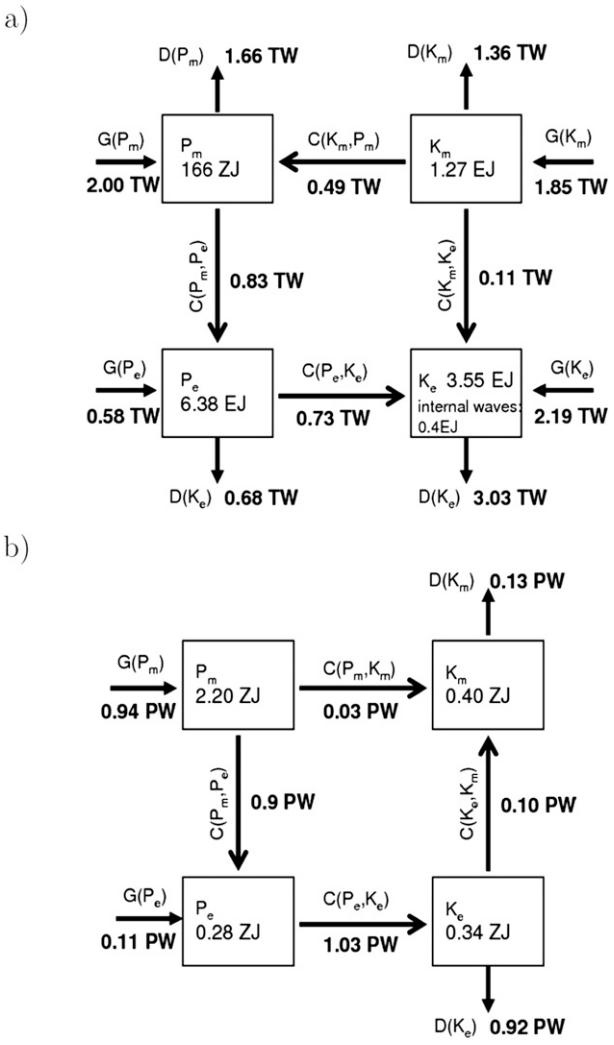

FIG. 13. LEC for the STORM/NCEP (top) ocean and (bottom) the atmosphere (Li et al. 2007). Energy reservoirs are in exajoules (EJ, 10^{18}) and zettajoules (ZJ, 10^{21}), rates of generation, dissipation, and conversion in terawatts (TW, 10^{12}) and petawatts (PW, 10^{15}). The notion ''internal waves'' in the box of oceanic K_e denotes the portion of K_e related to variations at frequencies larger than f. Values of Li et al. are transformed into watts and joules by multiplying with the surface area of the earth of 5.1×10^{14} m^2.

orders of magnitude smaller than those in Fig. 13b. Also the relative magnitudes of the reservoirs are different. In the ocean, P_e is the largest and amounts to 6.4 EJ, followed by K_e of 3.6 EJ and K_m of 1.3 EJ. In the atmosphere, K_m is the largest, followed by K_e and then P_e.

Regarding generation and conversion rates, the two LECs in Fig. 13 reveal one common feature and two striking differences. Common in both the atmosphere and the ocean is the pronounced baroclinic pathway $P_m \rightarrow P_e \rightarrow K_e$ characterized by a conversion from the mean available potential energy to the eddy available potential energy [$C(P_m, P_e)$] that has about the same magnitude as the conversion from the eddy potential energy to the eddy kinetic energy [$C(P_e, K_e)$]. The related power amounts to about 1 TW in the ocean and about 1 PW (peta watts = 10^{15} watts) in the atmosphere. In the ocean, the similarity between the spatial distributions of negative values $c(p_e, p_m)$ in Fig. 8 and positive values of $c(p_e, k_e)$ in Fig. 9 demonstrates that the two conversions occur hand in hand. As in the atmosphere, oceanic mesoscale eddies are, to a large extent, generated by baroclinic instability via the pathway $P_m \rightarrow P_e \rightarrow K_e$.

The first difference between the atmospheric and oceanic LEC concerns the rates of generation and dissipation, in particular those of P_m, K_m, and K_e, relative to the conversion rates to and from these reservoirs. The generation and dissipation rates are much stronger than the conversion rates in the ocean than in the atmosphere. Regarding P_m, K_m, and K_e in the ocean, the rates of generation and dissipation are about two times or more larger than the conversions (Fig. 13a). Thus, P_m, K_m, and K_e in the ocean are, to a first approximation, isolated, meaning that generation essentially balances dissipation. For the atmosphere, by contrast, the conversion terms are comparable or even larger than the respective generation and dissipation rates (Fig. 13b). This difference suggests that the generation and dissipation of P_m, K_m, and K_e in the ocean dominate the exchanges between the energy reservoirs via the oceanic circulation. In particular, the time-mean circulation in the ocean is to a first approximation determined by the surface forcing, with its interaction with mesoscale eddies being less important than the respective interaction in the atmosphere.

This difference in LEC directly results from the different power suppliers for the atmosphere and for the ocean. For the ocean, the power is mainly supplied by the winds. Of the total power input of 6.6 TW, about 60% comes from the winds and 40% originates from the buoyancy forcing. A considerable part of the kinetic energy of the ocean circulation can be forced by the winds without directly invoking the buoyancy forcing. By contrast, the atmosphere is forced by differential heating via radiative heat fluxes solely and there is no net mechanical power input. The kinetic energy of the atmosphere relies completely on the ability of the atmospheric circulation to transform available potential energy into kinetic energy. Even though this difference in power supplier for the two fluids is known and some direct consequences of this difference are expected, the present estimate of the oceanic LEC allows a quantification of the supplier and the relation of the external

power supplier to the conversion rates via the circulation in the ocean.

It should be noted that $G(P_m)$ and $G(P_e)$ in Fig. 13b are obtained by assuming no dissipation of P_m and P_e via diffusion, as it is done in almost all other estimates of the atmospheric LEC. The assumption is needed since for the atmosphere $G(P_m)$ and $G(P_e)$ cannot be easily estimated from radiative heat fluxes and are hence evaluated by balancing the corresponding conversion rates. Such an evaluation works only if the dissipation is assumed to be zero, so that the rate of generation is the only unknown. Thus, care should be taken regarding the relation of the external power supplier to the conversion rates via the circulation in the atmosphere.

The second difference between the atmospheric and oceanic LEC concerns the two conversion terms connected to the mean kinetic energy K_m [i.e., $C(K_m, P_m)$ and $C(K_m, K_e)$]. Both conversions are relatively strong and directed away from K_m in the ocean, but relatively weak and directed toward K_m in the atmosphere. The oceanic time-mean circulation, being fueled by the winds, converts its kinetic energy into the mean available potential energy by Ekman pumping. This conversion, which amounts to about 0.5 TW, substantially facilitates density differences and hence the mean available potential energy from which the baroclinic pathway originates. The oceanic time-mean circulation converts also its kinetic energy into the eddy kinetic energy. Overall, the main power pathway is notably affected and changed from $P_m \rightarrow P_e \rightarrow K_e \rightarrow K_m$ in the atmosphere, due to the dominance of the differential heating in generating P_m, to $K_m \rightarrow P_m \rightarrow P_e \rightarrow K_e$ and $K_m \rightarrow K_e$ in the ocean, due to the dominance of the winds in generating K_m. It is this change in the pathway that distinguishes the ocean as not being an heat engine.

The importance of the wind forcing in determining the direction of $C(P_m, k_m)$ and $C(K_e, K_m)$ is further underlined by the vertical profile of the area integrals of $c(p_m, k_m)$ and $c(k_e, k_m)$. According to Fig. 11 and Fig. 12, conversions are directed away from k_m, as characterized by negative values of $c(p_m, k_m)$ and $c(k_e, k_m)$ in the upper two to three km, where the effect of the winds is more prominent. The horizontal distribution of the mean vertical velocity indicates that negative values of $c(p_m, k_m)$ are due, to a considerable extent, to the wind-induced upwelling of denser water masses in the Southern Ocean.

9. Summary

We present here an estimate of the LEC for the World Ocean derived from a multidecadal simulation performed with the tripolar MPI-OM model at 0.1° resolution driven by the 6-hourly NCEP reanalysis data. The results, both those concerning the energy reservoirs (except for P_m) and those concerning the pathways within the LEC, are not sensitive to the choice of the reference density used to define the available potential energy, although several approximations are needed to derive the oceanic LEC.

Regarding the oceanic energy reservoirs we find the following.

- The mean kinetic energy, which amounts to a total of 1.3 EJ, is highly inhomogeneously distributed, with the most energetic motions being concentrated in sharp boundary currents and fine filaments.
- The eddy kinetic energy, which amounts to a total of 3.5 EJ, is more smoothly spread out and is almost three times stronger than the mean kinetic energy.
- For the time-varying circulation, the available potential energy P_e is larger than the kinetic energy K_e and reaches 6.4 EJ.

Regarding the pathways within the oceanic LEC we find the following.

1) Baroclinic instability is the main mechanism in converting the mean available potential energy into the eddy kinetic energy in the ocean. The total rate of this conversion amounts to 0.7–0.8 TW.
2) The oceanic energy reservoirs (in particular P_m, K_m, and K_e) are, to a first approximation, isolated, meaning that the generation balances, to a large extent, the dissipation, with the internal conversions to and from these reservoirs being less important. Overall the total power input to the ocean amounts to 6.6 TW, of which about 4 TW originates from the winds and the rest from the surface buoyancy forcing.
3) The power is transferred away from K_m, mainly via the pathway $K_m \rightarrow P_m \rightarrow P_e \rightarrow K_e$ with the conversion from K_m to P_m reaching about 0.5 TW, but also via the conversion from K_m to K_e, amounting about 0.1 TW.
4) The total dissipation of the kinetic energy amounts 4.4 TW, with about 70% being related to the dissipation of the eddy kinetic energy.

The first feature concerning the baroclinic instability is common for the LEC in both the atmosphere and the ocean. The second and third feature underline the differences between the atmospheric and oceanic LEC. In particular, the second feature implies that the general circulation in the ocean, as characterized by the mean kinetic energy K_m and the mean density differences in form of P_m, is to a first approximation supported by the

winds (Ekman pumping) and the surface buoyancy forcing, rather than by the activity of the interior mesoscale eddies. This contrasts the picture for the atmosphere in which the atmospheric general circulation is tightly coupled to synoptic disturbances. The third feature answers the question of what characterizes the ocean as not being a heat engine. The ''fuel'' that is needed to drive the baroclinic pathway is not only supplied by the surface buoyancy forcing, but also by the winds and via the conversion from K_m to P_m. The importance of the wind forcing relative to the buoyancy forcing for the oceanic general circulation is further underlined by the fourth feature suggesting that the winds could supply sufficient mechanical power for interior mixing needed to maintain the deep circulation. By contrast, there is no net mechanical energy input to the atmosphere, the conversion between K_m and P_m is almost absent, and the atmospheric baroclinic pathway is supported solely by the differential heating. Thus, if the atmosphere is considered as a heat engine that operates between heat sources at low latitudes near the surface and sinks at high latitudes in the upper troposphere, thereby converting thermal energy into mechanical energy, the ocean should be considered as a windmill that converts the wind energy into rotational energy of the eddies, or even as a refrigerator that uses the wind energy to generate, via Ekman pumping, temperature differences.

Acknowledgments. Computing resources were provided by the German Climate Computing Center (DKRZ). Irina Fast was financially supported by the CliSAP Cluster of Excellence of the University Hamburg. The STORM/NCEP simulation is part of the German STORM consortium project. It is acknowledged by various institutions inside Germany in general and by Institute of Coastal Research of the Helmholtz Zentrum Geestacht and Alfred Wegener Institute for Polar and Marine Research through their financial support in particular. Thanks also to Kenji Shimizu for reviewing the manuscript.

APPENDIX

Lorenz Energy Cycle Derived from the Primitive Equations for the Ocean

Appendix section a gives the momentum and the density equation needed for the derivation of the LEC. The momentum equation is standard, but the density equation has to be derived from the equations of potential temperature and salinity. Also listed in the first section are the assumptions that are made to ensure the derivation of manageable equations of available potential energy of the time-mean and time-varying circulation. Appendix sections b and c give the equations of kinetic and available potential energy per unit volume, respectively.

a. The primitive equations

For a primitive system, the momentum equation reads

$$\frac{d\mathbf{u}_h}{dt} + f\mathbf{k}\times\mathbf{u}_h = -\frac{1}{\rho_o}\nabla_h p + \frac{\partial\tau}{\partial z}, \tag{A1}$$

where $\mathbf{u}_h$ indicates the horizontal velocity vector,

$$\frac{d}{dt} = \frac{\partial}{\partial t} + \mathbf{u}_h\cdot\nabla + w\frac{\partial}{\partial z},$$

∇_h is the horizontal nabla operator, w the vertical velocity component, $\rho_o = 1025\ \text{kg m}^{-3}$, p is pressure, and $\tau = (\tau_x, \tau_y)$ is the vertical flux of horizontal momentum vector. The density equation can be derived from the equations of potential temperature θ and salinity S,

$$\frac{d\theta}{dt} = \frac{\partial J}{\partial z}, \tag{A2}$$

$$\frac{dS}{dt} = \frac{\partial G}{\partial z}, \tag{A3}$$

and the condition

$$\frac{d\rho}{dt} = \left(\frac{\partial\rho}{\partial\theta}\right)_{S,p}\frac{d\theta}{dt} + \left(\frac{\partial\rho}{\partial S}\right)_{\theta,p}\frac{dS}{dt} + \left(\frac{\partial\rho}{\partial z}\right)_{S,\theta}w \tag{A4}$$

that follows the equation of state $\rho = \rho(S, \theta, z)$. Here, J and G denote the vertical eddy fluxes of temperature and salt resulting from air–sea exchange. Other eddy fluxes, presented by the parameterizations in a state-of-the-art GCM, are neglected. Substituting Eqs. (A2) and (A3) into Eq. (A4) yields

$$\frac{\partial\rho}{\partial t} + \mathbf{u}_h\cdot\nabla_h\rho + w\left[\frac{\partial\rho}{\partial z} - \left(\frac{\partial\rho}{\partial z}\right)_{S,\theta}\right] = \left(\frac{\partial\rho}{\partial\theta}\right)_{S,p}\frac{\partial J}{\partial z} + \left(\frac{\partial\rho}{\partial S}\right)_{\theta,p}\frac{\partial G}{\partial z}.$$

Using the relation

$$\frac{\partial\varrho}{\partial z} = \frac{\partial\rho}{\partial z} - \left(\frac{\partial\rho}{\partial z}\right)_{S,\theta}, \tag{A5}$$

where $\varrho/\partial z$ indicates the vertical derivative of local potential density, the above equation reduces to

$$\frac{\partial \rho}{\partial t} + \mathbf{u}_h \cdot \nabla_h \rho + w \frac{\partial \varrho}{\partial z} = \left(\frac{\partial \rho}{\partial \theta}\right)_{S,p} \frac{\partial J}{\partial z} + \left(\frac{\partial \rho}{\partial S}\right)_{\theta,p} \frac{\partial G}{\partial z}. \quad \text{(A6)}$$

One important assumption made in our formulation of LEC is

$$\frac{\partial \varrho}{\partial z} \simeq \frac{\partial \langle \overline{\varrho} \rangle}{\partial z} \equiv n_o(z), \quad \text{(A7)}$$

where brackets denote the area mean. Thus, the vertical gradient of the local potential density is assumed to be constant at each level. Without Eq. (A7), it will be difficult to obtain a closed LEC. New terms, which result from the spatial variations of n_o and are likely related to conversions to other forms of (potential) energy, have to be included into Eqs. (A13) and (A14). In addition to Eq. (A7), we also assume that the temporal variations of the two expansion coefficients, $(\partial\rho/\partial\theta)_{S,p}$ and $(\partial\rho/\partial S)_{\theta,p}$, can be neglected and be approximated by

$$\left(\frac{\partial \rho}{\partial \theta}\right)_{S,p} \simeq \left(\frac{\partial \overline{\rho}}{\partial \theta}\right)_{S,p} \equiv \alpha_o(\lambda, \varphi, z), \quad \text{and} \quad \text{(A8)}$$

$$\left(\frac{\partial \rho}{\partial S}\right)_{\theta,p} \simeq \left(\frac{\partial \overline{\rho}}{\partial S}\right)_{\theta,p} \equiv \beta_o(\lambda, \varphi, z). \quad \text{(A9)}$$

Using Eq. (A7)–Eq. (A9), we obtain the approximated density equation for the primitive system

$$\frac{\partial \rho}{\partial t} + \mathbf{u}_h \cdot \nabla_h \rho + n_o w = \alpha_o \frac{\partial J}{\partial z} + \beta_o \frac{\partial G}{\partial z}. \quad \text{(A10)}$$

b. Equations of mean and eddy kinetic energy

The equation of mean kinetic energy per unit volume is obtained by multiplying the zonal and meridional components of Eq. (A1) with $\overline{u}$ and $\overline{v}$, and summing up and averaging the results over time. We find

$$\begin{aligned}\frac{\partial k_m}{\partial t} + \nabla \cdot (k_m \overline{\mathbf{u}}) + \nabla \cdot (\rho_o \overline{u}\overline{u'\mathbf{u}'}) + \nabla \cdot (\rho_o \overline{v}\,\overline{v'\mathbf{u}'}) + \nabla \cdot (\overline{p}\overline{\mathbf{u}}) \\ = \rho_o \overline{u'\mathbf{u}'} \cdot \nabla \overline{u} + \rho_o \overline{v'\mathbf{u}'} \cdot \nabla \overline{v} - g\overline{\rho}\,\overline{w} \\ + \frac{\partial}{\partial z}(\overline{\tau_x}\,\overline{u} + \overline{\tau_y}\,\overline{v}) - \epsilon(k_m), \end{aligned} \quad \text{(A11)}$$

where k_m denotes the kinetic energy per unit volume, $\mathbf{u} = (\mathbf{u}_h, w) = (u, v, w)$, and $\nabla = (\nabla_h, \partial/\partial z)$. Flux-gradient relations $\tau_x = \rho_o \nu \partial \overline{u}/\partial z$ and $\tau_y = \rho_o \nu \partial \overline{v}/\partial z$ are assumed to form the positive-definite quantities

$$\epsilon(k_m) = \rho_o \nu \left(\frac{\partial \overline{u}}{\partial z}\right)^2 + \rho_o \nu \left(\frac{\partial \overline{v}}{\partial z}\right)^2.$$

To obtain the equation of eddy kinetic energy k_e, the zonal and meridional components of Eq. (A1) are multiplied with u' and v', and the results are summed up and averaged over time. One finds

$$\begin{aligned}\frac{\partial k_e}{\partial t} + \nabla \cdot (k_e \overline{\mathbf{u}}) + \nabla \cdot \left[\frac{\rho_o}{2}\overline{\mathbf{u}'(u'^2 + v'^2)}\right] + \nabla \cdot \overline{p'\mathbf{u}'} \\ = -\rho_o \overline{u'\mathbf{u}'} \cdot \nabla \overline{u} - \rho_o \overline{v'\mathbf{u}'} \cdot \nabla \overline{v} - g\overline{\rho' w'} \\ + \frac{\partial}{\partial z}(\overline{\tau_x' u'} + \overline{\tau_y' v'}) - \epsilon(k_e), \end{aligned} \quad \text{(A12)}$$

where flux-gradient relations are assumed to define $\epsilon_e(k_e) = \rho_o \nu (\partial u'/\partial z)^2 + \rho_o \nu (\partial v'/\partial z)^2$.

Integrating Eqs. (A11) and (A12) over the entire ocean leads to Eqs. (8) and (9). Note that the volume integrals of the nabla-terms on the lhs of Eqs. (A11) and (A12) vanish.

c. Equations of mean and eddy available potential energy

The equation of mean available potential energy per unit volume is obtained by multiplying Eq. (A10) with $-(g/n_o)\overline{\rho}^*$, and averaging the result over time. We find

$$\begin{aligned}\frac{\partial p_m}{\partial t} + \overline{\mathbf{u}}_h \cdot \nabla_h p_m - \frac{g}{n_o} \nabla_h \cdot (\overline{\rho}^* \overline{\mathbf{u}_h' \rho^{*\prime}}) \\ = -\frac{g}{n_o} \overline{\rho^{*\prime} \mathbf{u}_h'} \cdot \nabla_h \overline{\rho}^* + g\overline{w}\,\overline{\rho}^* - g\frac{\alpha_o}{n_o}\frac{\partial}{\partial z}\overline{J}\,\overline{\rho}^* \\ - g\frac{\beta}{n_o}\frac{\partial}{\partial z}\overline{G}\,\overline{\rho}^* - \epsilon(p_m). \end{aligned} \quad \text{(A13)}$$

The dissipation term $\epsilon(p_m)$ arises again from flux-gradient relations.

The equation of eddy available potential energy p_e is obtained by multiplying Eq. (A10) by $-(g/n_o)\rho^{*\prime}$, and averaging the result over time. We find

$$\begin{aligned}\frac{\partial p_e}{\partial t} + \overline{\mathbf{u}}_h \cdot \nabla_h p_e + \overline{\mathbf{u}_h' \cdot \nabla_h p_e} \\ = \frac{g}{n_o} \overline{\mathbf{u}' \rho^{*\prime}} \cdot \nabla \overline{\rho}^* + g\overline{w' \rho^{*\prime}} - g\frac{\alpha_o}{n_o}\frac{\partial}{\partial z}\overline{\rho^{*\prime} J'} \\ - g\frac{\beta_o}{n_o}\frac{\partial}{\partial z}\overline{\rho^{*\prime} G'} - \epsilon(p_e). \end{aligned} \quad \text{(A14)}$$

The dissipation term $\epsilon(p_e)$ arises from flux-gradient relations. By choosing ρ_{ref} as a constant in both time and space, $\nabla\overline{\rho}^* = \nabla\overline{\rho}$.

Integrating Eqs. (A13) and (A14) over the ocean volume and neglecting the integral of the second and the third term on lhs of Eqs. (A13) and (A14), leads to Eqs. (6) and Eq. (7). Note that as discussed in section 3, the second term on the rhs of Eq. (A14) equals the negative of the third term on the rhs of Eq. (A12), and the area integral of the second term on the rhs of Eq. (A13) equals the area integral of the negative of the third term on the rhs Eq. (A11).

Note also that in contrast to Eqs. (A11) and (A12), which are derived from the model momentum equations more or less without any further approximation, Eqs. (A13) and (A14) result from a series of approximations, starting the density equation Eq. (A10), which makes use of Eq. (A7), to the assumptions of the smallness of the second and the third terms on the lhs of Eqs. (A13) and (A14).

REFERENCES

Böning, C. W., and A. J. Semtner, 2001: High-resolution modelling of the thermohaline and wind-driven circulation. *Ocean Circulation and Climate,* G. Siedler, J. Church, and J. Gould, Eds., Academic Press, 59–77.

Cox, M. D., 1985: An eddy resolving model of the ventilated thermocline. *J. Phys. Oceanogr.,* **15,** 1312–1324.

Ferrari, R., and C. Wunsch, 2009: Ocean circulation kinetic energy: Reservoirs, sources, and sinks. *Annu. Rev. Fluid Mech.,* **41,** 253–282.

——, and ——, 2010: The distribution of eddy kinetic and potential energies in the global ocean. *Tellus,* **62A,** 92–108.

Hernández-Deckers, D., and J.-S. von Storch, 2010: Energetics responses to increases in greenhouse gas concentration. *J. Climate,* **23,** 3875–3887.

——, and ——, 2011: The energetics response to a warmer climate: Relative contribution from the transient and stationary eddies. *Earth Syst. Dyn.,* **2,** 105–120.

Huang, R. X., 2004: Ocean energy flows. *Encyclopedia of Energy,* Vol. 4, Elsevier, 497–509.

Jochum, M., P. Malanotte-Rizzoli, and A. Busalacchi, 2004: Tropical instability waves in the Atlantic Ocean. *Ocean Modell.,* **7,** 145–163.

Johnson, D., 2000: Entropy, the Lorenz energy cycle and climate. *General Circulation Model Development: Past, Present and Future,* D. Randall, Ed., Academic Press, 659–720.

Jungclaus, J. H., and Coauthors, 2006: Ocean circulation and tropical variability in the coupled ECHAM5/MPI-OM. *J. Climate,* **19,** 3952–3972.

Kalnay, E., and Coauthors, 1996: The NCEP/NCAR 40-Year Reanalysis Project. *Bull. Amer. Meteor. Soc.,* **77,** 437–471.

Lee, M.-M., A. J. G. Nurser, A. C. Coward, and B. A. De Cuevas, 2007: Eddy advective and diffusive transports of heat and salt in the Southern ocean. *J. Phys. Oceanogr.,* **37,** 1376–1393.

Li, L., A. P. Ingersoll, X. Jiang, D. Feldman, and L. Y. Yuk, 2007: Lorenz energy cycle of the global atmosphere based on reanalysis datasets. *Geophys. Res. Lett.,* **34,** L16813, doi:10.1029/2007GL029985.

Lorenz, E. N., 1955: Available potential energy and the maintenance of the general circulation. *Tellus,* **7,** 157–167.

Lucarini, V., 2009: Thermodynamic efficiency and entropy production in the climate system. *Phys. Rev.,* **80E,** 021118, doi: 10.1103/PhysRevE.80.021118.

——, and F. Ragone, 2011: Energetics of climate models: Net energy balance and meridional enthalpy transport. *Rev. Geophys.,* **49,** RG1001, doi:10.1029/2009RG000323.

Maltrud, M. E., and J. L. McClean, 2005: An eddy resolving global 1/10° ocean simulation. *Ocean Modell.,* **8,** 31–54.

——, F. O. Bryan, and S. Peacock, 2010: Boundary impulse response functions in a century-long global eddying ocean simulation. *Environ. Fluid Mech.,* **10,** 275–295.

Masumoto, Y., and Coauthors, 2004: A fifty-year eddy-resolving simulation of the world Ocean—Preliminary outcomes of OFES (OGCM for the Earth Simulator). *J. Earth Simul.,* **1,** 35–56.

Maximenko, N. A., B. Bang, and H. Sasaki, 2005: Observational evidence of alternating zonal jets in the world ocean. *Geophys. Res. Lett.,* **32,** L12607, doi:10.1029/2005GL022728.

Munk, W., and C. Wunsch, 1998: Abyssal recipes II: Energetics of tidal and wind mixing. *Deep-Sea Res.,* **45,** 1976–2009.

Olbers, D., J. Willebrand, and C. Eden, 2012: *Ocean Dynamics.* Springer Verlag, 199 pp.

Oort, A. H., and J. P. Peixoto, 1983: Global angular momentum and energy balance requirements from observations. *Advances in Geophysics,* Vol. 25, Academic Press, 355–490.

Peixoto, J. P., and A. H. Oort, 1992: *Physics of Climate.* American Institute of Physics, 520 pp.

Röske, F., 2006: A global heat and freshwater forcing dataset for ocean models. *Ocean Modell.,* **11,** 235–297.

Sandström, J. W., 1908: Dynamische versuche mit Meerwasser. *Ann. Hydrogr. Martimen Meteor.,* **36,** 6–23.

——, 1916: Meteorologische Studien in Schwedischen Hochgebirge. Goteborgs Kungl. Vensk. Vitterh.-Samh. *Handingar,* **27,** 1–48.

Sasaki, H., and Coauthors, 2004: A series of eddy-resolving ocean simulations in the world ocean: OFES (OGCM for the Earth Simulator) project. *Proc. OCEANS '04,* Kobe, Japan, IEEE, 1535–1541.

——, M. Nonaka, Y. Masumoto, Y. Sasai, H. Uehara, and H. Sakuma, 2008: An eddy-resolving hindcast simulation of the quasiglobal ocean from 1950 to 2003 on the Earth Simulator. *High Resolution Numerical Modelling of the Atmosphere and Ocean,* K. Hamilton and W. Ohfuchi, Eds., Springer, 157–185.

Scharffenberg, M., and D. Stammer, 2010: Seasonal variations of the large-scale geostrophic flow field and eddy kinetic energy inferred from the TOPEX/Poseidon and *Jason-1* tandem mission data. *J. Geophy. Res.,* **115,** C02008, doi:10.1029/2008JC005242.

Tailleux, R. G. J., 2009: On the energetics of stratified turbulent mixing, irreversible thermodynamics, Boussinesq models and the ocean heat engine controversy. *J. Fluid Mech.,* **638,** 339–382, doi:10.1017/S002211200999111X.

——, 2010: Entropy versus APE production: On the buoyancy power input in the oceans energy cycle. *Geophys. Res. Lett.,* **37,** L22603, doi:10.1029/2010GL044962.

von Storch, J.-S., H. Sasaki, and J. Marotzke, 2007: Wind-generated power input to the deep ocean: An estimate using a 1/10 degree general circulation model. *J. Phys. Oceanogr.,* **37,** 657–672.

Wunsch, C., 1998: The work done by the wind on the oceanic general circulation. *J. Phys. Oceanogr.,* **28,** 2332–2340.

——, and R. Ferrari, 2004: Vertical mixing, energy, and the general circulation of the oceans. *Annu. Rev. Fluid Mech.,* **36,** 281–314.